

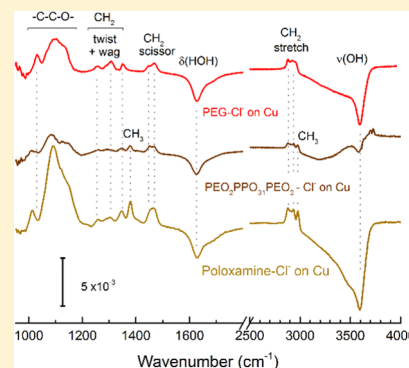
## SEIRAS Study of Chloride-Mediated Polyether Adsorption on Cu

Guo-Kun Liu,<sup>†</sup> Shouzhong Zou,<sup>‡</sup> Daniel Josell, Lee J. Richter, and Thomas P. Moffat\*

Materials Measurement Laboratory, National Institute of Standards and Technology, Gaithersburg, Maryland 20899, United States

## Supporting Information

**ABSTRACT:** Surface-enhanced infrared absorption spectroscopy is used to examine the co-adsorption of a selection of polyethers with  $\text{Cl}^-$  under conditions relevant to superconformal Cu electrodeposition in  $\text{CuSO}_4\text{--H}_2\text{SO}_4$  electrolytes. In 0.1 mol/L  $\text{H}_2\text{SO}_4$ , a potential-dependent mixed  $\text{SO}_4^{2-}\text{--H}_3\text{O}^+/\text{H}_2\text{O}$  layer forms on weakly textured (111) Cu thin-film surfaces. With the addition of 1 mmol/L NaCl, the  $\text{SO}_4^{2-}\text{--H}_3\text{O}^+/\text{H}_2\text{O}$  adlayer is displaced and rapidly replaced by an ordered halide layer that disrupts the adjacent solvent network, leading to an increase in non-hydrogen-bonded water that makes the interface more hydrophobic. The altered wetting behavior facilitates co-adsorption of polyethers, such as poly(ethylene glycols), polyoxamers, or polyoxamines. Interfacial water is displaced by co-adsorption of the hydrophobic polymer segments on the  $\text{Cl}^-$ -terminated surface, while the hydrophilic ether oxygens are available for hydrogen bond formation with the solvent. The combined polyether- $\text{Cl}^-$  layer serves as an effective suppressor of the Cu electrodeposition reaction by limiting access of  $\text{Cu}_{\text{aq}}^{2+}$  to the underlying metal surface. This insight differs from previous work which suggested that polymer adsorption is mediated by  $\text{Cu}^+\text{--ether}$  binding.



## INTRODUCTION

Cu electrodeposition is a key process used in the fabrication of microelectronic circuitry ranging from deep submicrometer logic and memory interconnects to micron-scale through-silicon vias (TSV) for three-dimensional chip stacking. The success of the process stems from surfactant additives that enable void- and seam-free, bottom-up “superfilling” of recessed surface features, such as trenches and vias.<sup>1,2</sup> For submicrometer features, superconformal growth involves competitive adsorption between polyethers (e.g., poly(ethylene glycol) (PEG) and/or its derivatives) that suppress metal deposition and sulfonate-terminated alkyl disulfides and/or related thiols that accelerate Cu deposition.<sup>3,4</sup> For larger-scale features, such as TSV, extreme bottom-up filling can occur due to disruption of the polymer suppressor layer by positive feedback with the metal deposition reaction itself.<sup>5–8</sup>

In prototypical acidic  $\text{CuSO}_4$  electrolytes,  $\text{Cl}^-$  is an essential additive influencing the co-adsorption and operation of both polyether inhibitors and sulfonate-terminated alkyl disulfide accelerator species.<sup>3–20</sup> In situ scanning tunneling microscopy (STM) and surface X-ray scattering (SXS) measurements have revealed a great deal about the structure and step dynamics associated with potential-dependent phase transitions of the chemisorbed anions,  $\text{SO}_4^{2-}$  and  $\text{Cl}^-$ , on low-index Cu surfaces.<sup>21–31</sup> At technically relevant concentrations,  $\text{Cl}^-$  displaces  $\text{SO}_4^{2-}$  from the Cu surface and facilitates an increase in the rate of the  $\text{Cu}^{2+}/\text{Cu}^+$  inner sphere electron-transfer reaction.<sup>32,33</sup> The addition of PEG ( $M_w = 3400$  g/mol) to the electrolyte suppresses the Cu deposition rate by 2 orders of magnitude relative to the  $\text{H}_2\text{SO}_4\text{--CuSO}_4\text{--Cl}^-$  solution.<sup>3–17</sup> However, in the absence of halide, negligible inhibition of

metal deposition is observed, demonstrating that  $\text{Cl}^-$  is required for the polyether suppressor to function.<sup>9–17</sup>

A variety of in situ measurements have been used to examine the relative roles of  $\text{Cl}^-$  and  $\text{Cu}^+$  in the formation and function of polyether suppressor layers. Ellipsometry measurements of the PEG- $\text{Cl}^-$  adlayer, in the absence of metal deposition, indicate that a thin ( $\approx 0.6$  nm) PEG layer is formed on top of the  $\text{Cl}^-$  adlayer while no polymer adsorption is evident in the absence of  $\text{Cl}^-$ .<sup>34</sup> An electrochemical quartz crystal microbalance (EQCM) study indicates that neither  $\text{Cu}^+$  nor  $\text{Cu}^{2+}$  is required to form the suppressor layer.<sup>35</sup> In contrast, other experimental studies have invoked  $\text{Cu}^+$  as the binding agent between the polymer ether oxygen and the halide-covered surface.<sup>10,36,37</sup> Among these, a surface-enhanced Raman spectroscopy study ascribed a vibrational feature at  $670\text{ cm}^{-1}$  to  $\text{Cu}^+$  mediating or binding the polyether oxygen to the  $\text{Cl}^-$ -covered surface in analogy to crown ether complexes and related solid-state poly(ethylene oxide) (PEO)-cation complexation.<sup>10,36</sup> The proposed crown ether conformation was used to explain the influence of PEG molecular weight on suppression and feature filling.<sup>10,38</sup> However, other Raman studies are at odds with the preceding result, with only weak and/or transient signals observed, which were most likely related to morphological instabilities that are known to hinder quantitative SERS.<sup>39,40</sup>

Imaging the suppressor layer by scanning tunneling microscopy (STM) and atomic force microscopy has proven challenging as tip scanning forces tend to disrupt the polymer

Received: July 12, 2018

Revised: August 29, 2018

Published: August 31, 2018

due to its modest monomeric binding energy; however, three recent STM studies provide evidence of the formation of two-dimensional (2D) PEG adlayers.<sup>41–43</sup> For small PEG oligomers, such as a 5-mer, an ordered ( $4 \times 4$ ) arrangement was imaged on top of  $\text{Cl}_{\text{ads}}/\text{Cu}_{\text{upd}}/\text{Pt}(111)$  surfaces with a nearest-neighbor modulation of the electron density of 1.1 nm. Increasing the tunneling current to bring the tip closer to the surface revealed the underlying  $\sqrt{3} \times \sqrt{3} R30^\circ \text{Cl}^-$  adlayer on top of the  $\text{Cu}_{\text{upd}}$  layer.<sup>42</sup> Attempts to image higher-molecular-weight polymers (PEG with  $M_w = 400, 600, \text{ and } 4000$ ) yielded irreproducible results, which was attributed to the interference between the polymer and the imaging tip. The difficulty in imaging is congruent with the collapsed sphere model derived from an EQCM study of PEG– $\text{Cl}^-$  adsorption on Cu as well as the loop-train-tail picture of polymer adsorption and more recent observation of the substantial adsorption–desorption dynamics of PEG at hydrophobic solid–liquid interfaces in the dilute coverage limit.<sup>11,44</sup> In contrast, a subsequent study of PEG ( $M_w = 6000$ ) adsorption on negatively charged Au in pH 3 sulfate electrolyte revealed a 2D monomolecular film exhibiting linear, possibly nematic, features within the surface plane consistent with individual PEG chains.<sup>43</sup> The planar nature of the arrangement indicates a significant polymer–surface interaction energy compared to the solvation energy of the polymer.<sup>45,46</sup> Unlike with Cu, STM and voltammetry indicate that halide adsorption is not necessarily required for PEG adsorption on Au, although EQCM and ellipsometry reveal conditions where halide is required.<sup>11,34,41,43</sup> The seemingly divergent observations suggest that a more complete understanding of PEG adsorption should consider both the state of charge and hydration of the respective surfaces.

Despite these prior efforts, molecular insight into the polymer–halide binding interaction and suppressor function is still lacking. The role of fluxional adsorption–desorption polymer dynamics in determining the leakage currents and breakdown events associated with the passivating layer is unknown. It is unclear if the suppressor layer operates by site blocking, i.e., simply limiting access of  $\text{Cu}^{2+}$  to the surface or is directly involved in the metal deposition reaction itself through interactions with the  $\text{Cu}^+$  reaction intermediate. Likewise, it is not clear whether  $\text{Cu}^+$  plays a role in binding the polymer to the halide adlayer. Studies of polyether adsorption in other, chemically distinct, systems suggest other possibilities. Among these, multisite noncovalent interactions with molecular solvation and interfacial water structure being perturbed by anion or cation co-adsorption is of particular relevance.<sup>47–49</sup> For example, PEG adsorption on negatively charged mica surfaces is thought to be mediated by differences in the hydration shells associated with co-adsorbing alkali–metal cations.<sup>47</sup> Similarly, reports of the assembly and mobility of PEG at hydrophobic solid–liquid interfaces point to the importance of wetting forces in understanding polyether adsorption.<sup>44,50,51</sup>

In situ vibrational spectroscopy techniques, such as sum frequency generation (SFG) and surface-enhanced infrared absorption spectroscopy (SEIRAS), enable direct probing of the molecular nature of interface hydration and its potential dependence.<sup>50–55</sup> Specifically, enhancement effects associated with nanostructured ultrathin-film electrodes enable SEIRAS to be combined with potential step and titration schemes to study the adsorption dynamics of ionic and molecular species at electrode surfaces. Herein, SEIRAS is used to examine co-

adsorption of prototypical polyether– $\text{Cl}^-$  additives that provide suppression during Cu electroplating.

## MATERIALS AND METHODS

SEIRAS measurements were performed using a Cu thin-film electrode supported on an optically polished Si prism (PIKE Technologies, Inc.<sup>49</sup>) in the Kretschmann attenuated total reflection (ATR) configuration. The prism was positioned within the spectrometer using a modified commercial attachment (VeeMAX II, PIKE Technologies, Inc. with an in-house-modified base plate to support the prism) with the incident and exit angles set to  $60^\circ$ . The Nicolet Magna-IR860 Fourier transform infrared spectrometer was equipped with a liquid  $\text{N}_2$ -cooled HgCdTe detector. Spectra were typically recorded at  $4 \text{ cm}^{-1}$  resolution with 100 interferometer scans co-added for an acquisition time of ca. 60 s. Measurements were conducted with unpolarized IR radiation, and the optical path of the spectrometer was purged with dry air from a gas generator or evaporated cryogenic  $\text{N}_2$  for at least 30 min prior to initiating the electrochemical experiments. The spectral region below  $900 \text{ cm}^{-1}$  was not accessible due to absorption in the Si prism as evident in the single-beam spectrum for the Si/air and Si/Cu/air interface shown in Figure S1a. The 20 nm Cu film was deposited on the prism surface by physical vapor deposition (PVD) via electron beam evaporation. As shown in Figure S1b, the Cu film is just past the onset of island coalescence, to take advantage of the percolation threshold being associated with the strongest enhancement of vibrational signals.<sup>56</sup> In a subset of experiments, a thin Ti adhesion layer was examined to improve the adhesion between Cu and  $\text{SiO}_2$ ; however, this resulted in an inverted spectral response that will be reported elsewhere. For electrochemical measurements, a cylindrical Kel-F chlorotrifluoroethylene cell was mounted on top of the horizontal working surface of the Cu-coated Si prism. Electrical contact to the perimeter of the film was provided by a thin annular Cu foil that was mechanically pressed against it by a Teflon-coated O-ring defining the outer diameter of the cell. A Pt coil counter electrode and a  $\text{Hg}/\text{Hg}_2\text{SO}_4/\text{K}_2\text{SO}_4(\text{sat'd})$  (saturated sulfate electrode (SSE)) reference electrode were used. All solutions were made with 18 M $\Omega$  cm water (Barnstead EasyPure UV). Commercially available chemicals were used for all experiments: analytical-grade  $\text{H}_2\text{SO}_4$  (Aldrich) and NaCl (Aldrich), poly(ethylene glycol), PEG<sub>77</sub> ( $M_w \text{ avg} \sim 3400$ , Aldrich), deuterated poly(ethylene oxide), dPEG ( $M_n \text{ avg} \sim 3450 \text{ max.}, 3200 \text{ min.}, M_w/M_n 1.08$ , Polymer Source), a poloxamer, poly(ethylene glycol)-*block*-poly(propylene glycol)-*block*-poly(ethylene glycol) PEO<sub>2</sub>-PPO<sub>31</sub>-PEO<sub>2</sub> ( $M_n \text{ avg} \sim 2000$ , Pluronic L-61, Aldrich), and a poloxamine, ethylenediamine tetrakis(propoxylate-*block*-ethoxylate)tetrol (PEO<sub>4</sub>PPO<sub>12</sub>)<sub>2</sub>ED(PPO<sub>12</sub>PEO<sub>4</sub>)<sub>2</sub> ( $M_n \text{ avg} \sim 3600$ , Tetronic 701, Aldrich). Schematic drawings of the respective polyethers are shown in Figure 1a.

A fresh Cu surface was prepared for each experimental run. Preparation involved the following sequence of steps: mechanical polishing of the Si prism with  $0.3 \mu\text{m}$  and then  $0.05 \mu\text{m}$  diamond paste, sonication in Caro's (piranha) solution (75 vol %  $\text{H}_2\text{SO}_4 + 25 \text{ vol } \% \text{H}_2\text{O}_2$ ), and drying in flowing  $\text{N}_2$  or Ar. The prepared crystal was placed in an electron beam evaporator and pumped overnight to a pressure  $\leq 2.7 \times 10^{-5} \text{ Pa}$  ( $2 \times 10^{-7} \text{ Torr}$ ). Additional Si wafer fragments were placed besides the Si prism to serve as reference and control specimens for X-ray photoelectron spectroscopy examination and voltammetric analysis. In a subset of

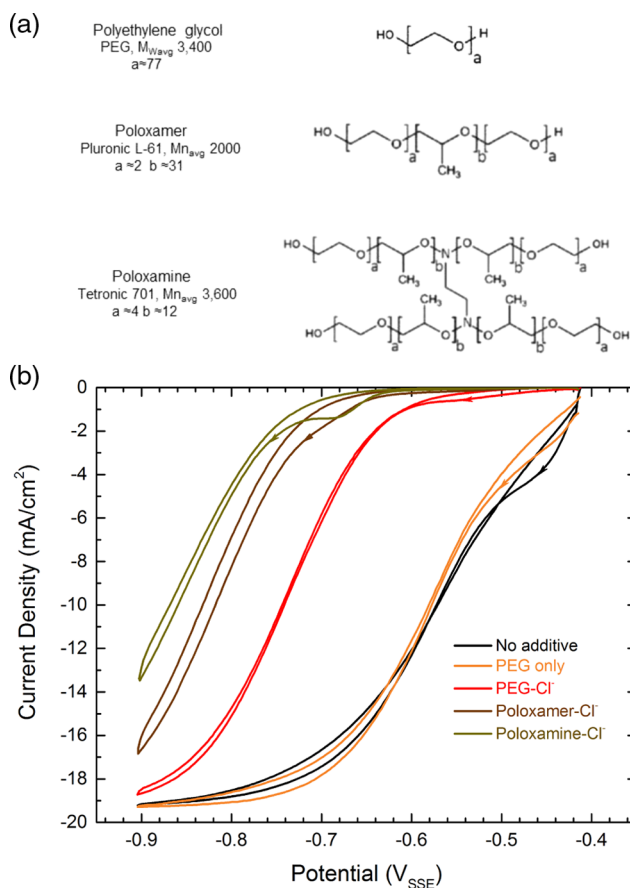


**Figure 1.** (a) Chemical structure of three polyether suppressors: PEG, poloxamer, and poloxamine. (b) Slow scan voltammetry (1 mV/s) of Cu deposition in the presence of the respective polymers and halide revealing the importance of co-adsorption and the chemistry and secondary structure of polyethers in the suppression of the Cu deposition (0.24 mol/L CuSO<sub>4</sub> + 1.8 mol/L H<sub>2</sub>SO<sub>4</sub> + 1 mmol/L NaCl + 80–90 μmol/L polymer).

experiments, the vacuum was further scrubbed prior to film deposition by evaporating Ti while the Si prism was protected by a shield. Metal deposition was initiated by turning the shielded Si prism, with its native oxide-coated surface, toward the Cu source. The rate of film growth was controlled and the final thickness was determined by quartz crystal monitors located in proximity to the prism substrate. The results presented in this paper focus on Cu films deposited at fixed rates of 0.1, 0.05, 0.01, or 0.006 nm/s. No distinctive SEIRAS features, nor trends, were associated with the deposition rate or vacuum conditions.

SEIRAS experiments were initiated with the addition of Arsparged 0.1 mol/L H<sub>2</sub>SO<sub>4</sub> electrolyte to the electrochemical cell. The Cu thin film and adjacent Hg/Hg<sub>2</sub>SO<sub>4</sub>/K<sub>2</sub>SO<sub>4</sub>(sat'd) (SSE) reference electrode were sequentially covered with the electrolyte, and potential control was established when the counter electrode subsequently made contact, which usually occurred within 1 s. Potential step and additive titration experiments were then performed. Typically, multiple spectra were collected for given electrochemical conditions to establish and verify time stability as a precondition for interpreting subsequent potential difference or titration experiments. Difference spectra are presented as absorbance *A*, defined as  $A = -\log(I_1/I_0)$ , where *I*<sub>1</sub> is the intensity of the reflected beam at the potential or concentration of interest and *I*<sub>0</sub> corresponds

to that at the specified reference condition. Positive bands correspond to increased adsorption cross section, indicating increased coverage and/or transition moment dipole due to altered orientation of the adsorbing species. Negative bands correspond to the opposite. Changes in the magnitude and shape of the absorption bands were quantified by peak deconvolution using the Voigt or Gaussian peak shape within the Origin 2016 analysis and graphing program.

## RESULTS AND DISCUSSION

Voltammetry for Cu deposition from a 0.24 mol/L CuSO<sub>4</sub> + 1.8 mol/L H<sub>2</sub>SO<sub>4</sub> electrolyte is shown in Figure 1b. The addition of Cl<sup>-</sup> and polyethers results in significant suppression of the deposition process due to the formation of a passivating polyether–Cl<sup>-</sup> layer that blocks access of Cu<sup>2+</sup> to the Cu surface. SEIRAS was used to examine adsorption of the individual components and their interactions to gain insight into the structure, dynamics, and function of the overlayer.

**SO<sub>4</sub><sup>2-</sup> Adsorption on Cu in H<sub>2</sub>SO<sub>4</sub>.** A cyclic voltammogram for a 20 nm PVD Cu film in 0.1 mol/L H<sub>2</sub>SO<sub>4</sub> is shown in Figure 2. Metal dissolution occurs at potentials positive of

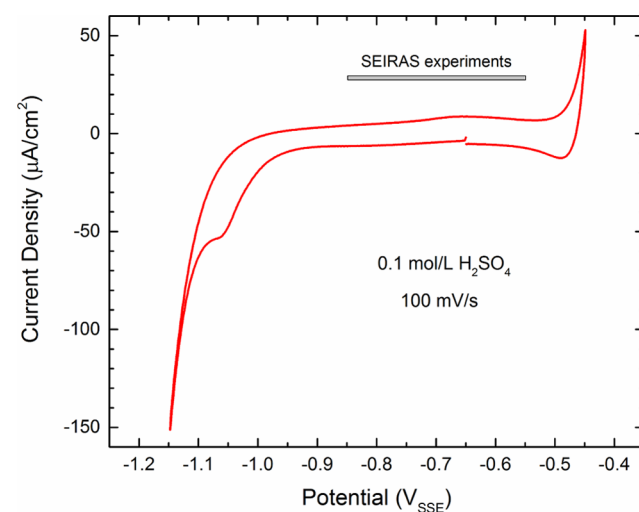


**Figure 2.** Cyclic voltammetry of a 20 nm PVD Cu film supported on air-formed SiO<sub>x</sub> on Si reveals waves related to anion adsorption and reconstruction. The inset gray band corresponds to the potential window examined by SEIRAS.

–0.5 V<sub>SSE</sub>, while proton reduction is evident at more negative potentials. For SEIRAS measurements, the potential was held at, or below, –0.55 V<sub>SSE</sub> to avoid film dissolution, while the limited adhesion strength of Cu to the oxide-covered Si prism hindered exploration in the hydrogen evolution region. Despite these limitations, the potential window examined (gray bar, inset) overlaps that used for superconformal deposition of Cu interconnects. The reduction wave at –1.050 V<sub>SSE</sub> and the anodic wave centered near –0.670 V<sub>SSE</sub> correspond to similar, albeit more well-defined, voltammetric waves previously reported for freshly prepared Cu(111) in a variety of electrolytes.<sup>25–27</sup>

Physical vapor deposition of face-centered cubic (fcc) metals on amorphous SiO<sub>x</sub> surfaces usually results in a (111) out-of-plane film texture. Accordingly, a brief review of prior STM and infrared reflection absorption spectroscopy (IRRAS) studies of Cu(111) in 5 mmol/L H<sub>2</sub>SO<sub>4</sub> is warranted.<sup>26,57,58</sup> At potentials >–0.8 V<sub>SSE</sub>, in the double-layer region, SO<sub>4</sub><sup>2-</sup>

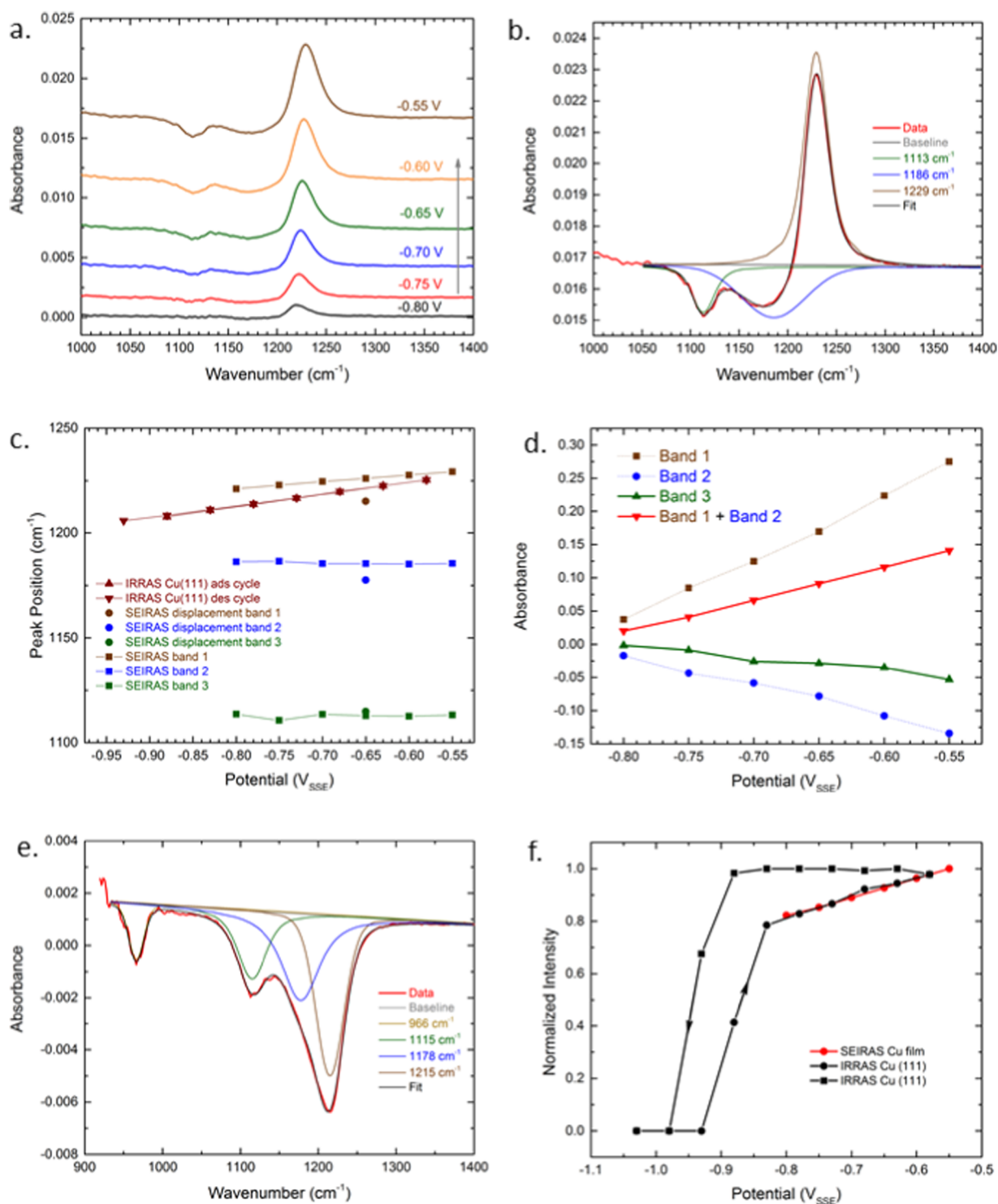


**Figure 3.** (a) SEIRAS spectra, referenced to  $-0.85 V_{SSE}$ , showing bands related to  $SO_4^{2-}$  adsorption on the Cu film in 0.1 mol/L  $H_2SO_4$ . (b) Example of spectral deconvolution in 1000–1400  $cm^{-1}$  region using three components. (c) The dominant  $SO_4^{2-}$  peak exhibits a Stark shift of  $33.1 cm^{-1} V^{-1}$  compared to  $55\text{--}60 cm^{-1} V^{-1}$  from an IRRAS study of Cu(111).<sup>58</sup> The red circle at  $-0.65 V_{SSE}$  represents the peak position of the displacement band due to halide addition (vide infra). (d) The intensity of the respective  $SO_4^{2-}$  spectral components, band 1 (1229  $cm^{-1}$ ) and band 2 (1186  $cm^{-1}$ ), are correlated and thus the sum (band 1 + band 2) is used for analysis. (e)  $SO_4^{2-}$  displacement spectrum following the addition of 1 mmol/L NaCl at  $-0.65 V_{SSE}$ . (f) Potential dependence of SEIRAS  $SO_4^{2-}$  data (band 1 + band 2) compared to IRRAS data for Cu(111).<sup>58</sup> The intensity of the potential difference data was offset by the  $SO_4^{2-}$  displacement spectra (e).

adsorption occurs rapidly, followed by a much slower reconstruction and expansion of the top Cu surface to form an ordered  $\sqrt{3} \times \sqrt{7} R19^\circ$  mixed  $SO_4^{2-} + H_5O_2^+$  adlayer.<sup>26</sup> Kinetic limitations on the interlayer Cu mass exchange needed

to form the  $SO_4^{2-}$ -covered reconstructed surface account for the slow ordering dynamics. At potentials  $< -0.9 V_{SSE}$ ,  $SO_4^{2-}$  desorption occurs accompanied by rapid relaxation to a  $1 \times 1$  Cu(111) metal surface. Repetitive rearrangements with

potential cycling result in significant roughening of the interface. The surface structure is highly sensitive to processing history with the formation of large ordered domains favored by slow potentiodynamic scan rates, or small potential steps, whereas poorly ordered layers are formed during more rapid  $\text{SO}_4^{2-}$  adsorption, as evidenced by in situ STM studies.<sup>26</sup> IRRAS measurements on Cu(111) revealed a potential-dependent  $\text{SO}_4^{2-}$  band, whose intensity increased in a monotonic, but nonlinear, fashion with potential.<sup>57,58</sup> At the same time, a linear Stark shift of  $55 \text{ cm}^{-1} \text{ V}^{-1}$ , from 1205 to  $1225 \text{ cm}^{-1}$ , was observed based on the reference spectra collected at a potential negative of the reduction wave that marks the lower limit of the “double layer” regime. The potential dependence of the  $\text{SO}_4^{2-}$  intensity, and thereby coverage, was hysteretic while the Stark shift was completely reversible.<sup>58</sup> Despite the kinetic constraint, the saturation IRRAS intensity and its vibrational energy were largely independent of adlayer ordering. There are no firm reports of ordered  $\text{SO}_4^{2-}$  layers on other low-index Cu surfaces in acidic media.

SEIRAS experiments on the thin PVD Cu films were initiated upon the addition of 0.1 mol/L  $\text{H}_2\text{SO}_4$  with the electrode poised at  $-0.65 \text{ V}_{\text{SSE}}$ . Individual spectra include substantial contributions from electrolyte species that lie beyond the double-layer region.<sup>53,56</sup> However, by taking the difference between sequential spectra collected at different potentials, or before and after titration of a dilute species, the contributions associated with bulk electrolyte species are effectively nulled and the sensitivity of SEIRAS to changes in interface species are revealed. For example, Figure S2 shows spectra referenced to a spectrum collected at  $-0.65 \text{ V}_{\text{SSE}}$ . The bands near  $1234 \text{ cm}^{-1}$  capture increased  $\text{SO}_4^{2-}$  coverage at  $-0.55 \text{ V}_{\text{SSE}}$  versus a net loss at  $-0.8 \text{ V}_{\text{SSE}}$ . Changes in the water-bending mode,  $\delta(\text{HOH})$ , near  $1650 \text{ cm}^{-1}$  and stretching modes,  $\nu(\text{OH})$ , between  $3200$  and  $3600 \text{ cm}^{-1}$  are also evident. The potential-dependent trends for adsorbed  $\text{SO}_4^{2-}$  were reproducible with potential cycling, as well as between independent experiments, while the water modes continued to evolve with cycling.

To determine the potential dependence of anion coverage, reference spectra are ideally taken at potentials that correspond to an “adsorbate-free” surface. The negative point of zero charge (pzc) of Cu, i.e.,  $-0.98$  to  $-1.36 \text{ V}_{\text{SSE}}$ , combined with the tendency of the Cu films to delaminate from the Si prism at such negative potentials made this difficult to implement.<sup>59</sup> As a result, difference spectra were referenced to the most negative value reliably examined, namely,  $-0.85 \text{ V}_{\text{SSE}}$ . Data collection was initiated immediately after stepping to the specified potential, and once acquisition was complete, typically within a minute, the potential was stepped in the positive direction, typically in 0.05 V increments, and the process repeated. As shown in Figure 3a, a monotonic increase in the intensity of the major  $\text{SO}_4^{2-}$  band at  $\approx 1225 \text{ cm}^{-1}$ , accompanied by a monotonic decrease in the smaller neighboring peak at  $1114 \text{ cm}^{-1}$ , occurs between  $-0.80$  and  $-0.55 \text{ V}_{\text{SSE}}$ . The complete spectra with the corresponding water-bending modes  $\delta(\text{HOH})$ , near  $1650 \text{ cm}^{-1}$ , and stretching modes  $\nu(\text{OH})$ , above  $3000 \text{ cm}^{-1}$ , are shown in Figure S3a. The bipolar characteristic associated with the dominant  $\sim 1225 \text{ cm}^{-1}$  band is related to the choice of reference potential, whereby the negative portion of the spectra reflects the Stark shift of species previously adsorbed at the reference potential. The spectra were fit to three peaks, as

shown in Figure 3b, with the peak wavenumber and intensity of the components summarized in Figure 3c,d, respectively. Among the spectral components, only the  $1205\text{--}1230 \text{ cm}^{-1}$  band (SEIRAS band 1) exhibits a Stark shift ( $\approx 33\text{--}35 \text{ cm}^{-1} \text{ V}^{-1}$ ). Arbitrary normalization of the potential difference spectra to that at  $-0.85 \text{ V}_{\text{SSE}}$ , combined with the absence of an obvious indication of saturated band intensity at the most positive potential, hinders determination of the absolute  $\text{SO}_4^{2-}$  coverage. Damage to the Cu film by faradaic reactions such as metal dissolution or hydrogen evolution precluded the use of an expanded potential range that might reveal saturation.

Potential difference spectra highlight changes in the intensity and frequency of the vibrational bands but obscure modes that have minimal potential dependence. Displacement reactions offer an alternative means to determine the  $\text{SO}_4^{2-}$  coverage. For Cu surfaces, halides are suitable candidates as they adsorb more strongly than  $\text{SO}_4^{2-}$ .<sup>21–27,60</sup> Addition of 1 mmol/L  $\text{Cl}^-$  to the electrolyte results in complete displacement of  $\text{SO}_4^{2-}$  at  $-0.65 \text{ V}_{\text{SSE}}$ , as revealed by the four negative titration bands in Figure 3e. In addition to the strong band centered at  $1215 \text{ cm}^{-1}$ , a second peak near  $1180 \text{ cm}^{-1}$  was necessary to fit the spectra, along with the smaller adjacent band near  $1115 \text{ cm}^{-1}$  and the solitary band at  $968 \text{ cm}^{-1}$ , close to the Si prism spectral cutoff. The combined integrated intensity of the  $1215$  and  $1180 \text{ cm}^{-1}$  desorption peaks (band 1 + band 2) in Figure 3e exceeds by a factor of 4–5, that seen in the potential difference spectra in Figure 3a. This indicates that a significant  $\text{SO}_4^{2-}$  coverage is present at the reference potential ( $-0.85 \text{ V}_{\text{SSE}}$ ) used to generate the difference spectra shown in Figure 3a. The potential difference spectra of Figure 3a are offset by the intensity loss spectrum (Figure 3e) for the titration displacement experiment at  $-0.65 \text{ V}_{\text{SSE}}$  to account for this nonzero coverage. The potential dependence of the combined  $1215$  and  $1180 \text{ cm}^{-1}$  bands derived from this procedure is scaled to the value at  $-0.55 \text{ V}_{\text{SSE}}$  and compared to the similarly scaled integrated intensity of the  $\approx 1215 \text{ cm}^{-1}$  band from the IRRAS study of Cu(111), as summarized in Figure 3f.<sup>58</sup> We note that the published Cu(111) spectra were also asymmetric and could be modeled by two correlated symmetric Voigt functions. As the respective SEIRAS and IRRAS measurements were performed in electrolytes with different  $\text{H}_2\text{SO}_4$  concentrations and reference electrodes, the potential axis for the Cu(111) literature data was offset, taking  $-0.680 \text{ V}_{\text{SSE}}$  to correspond to  $0.0 \text{ V}_{\text{RHE}}$ , for comparison of the coverage evolution with the present results. The black arrows in Figure 3f indicate the hysteresis observed between the adsorption and desorption processes for the Cu(111) IRRAS measurements.<sup>58</sup> The favorable overlap of the normalized intensity of the Cu thin-film data (sum of the  $1221\text{--}1229 \text{ cm}^{-1}$  (band 1) and  $1186 \text{ cm}^{-1}$  (band 2) components) with that for  $\text{SO}_4^{2-}$  adsorption on Cu(111) ( $1200\text{--}1225 \text{ cm}^{-1}$ ) is noteworthy. The steep increase in the  $1215 \text{ cm}^{-1}$  band intensity near  $-0.9 \text{ V}_{\text{SSE}}$  marks the onset of  $\text{SO}_4^{2-}$  adsorption, followed by the more gradual approach to saturation at more positive potential. The ca.  $30\text{--}38 \text{ cm}^{-1} \text{ V}^{-1}$  Stark shift of the dominant  $\approx 1225 \text{ cm}^{-1}$  peak in the Cu thin-film SEIRAS measurements, summarized in Figure 3c, differs from the  $60\text{--}55 \text{ cm}^{-1} \text{ V}^{-1}$  reported for Cu(111).<sup>57,58</sup> The peak band energy for  $\text{SO}_4^{2-}$  displaced by  $\text{Cl}^-$  at  $-0.65 \text{ V}_{\text{SSE}}$  (Figure 3e) is  $1215 \text{ cm}^{-1}$ , shifted slightly ( $-10 \text{ cm}^{-1}$ ) from the peak position observed in the potential difference spectra referenced to  $-0.85 \text{ V}_{\text{SSE}}$ . The respective experimental values at  $-0.65 \text{ V}_{\text{SSE}}$ , shown in Figure 3c, bracket those reported for Cu(111) while the anticorre-

lated nature of the 1221–1229  $\text{cm}^{-1}$  (band 1) and 1186  $\text{cm}^{-1}$  (band 2) components reflects convolution of coverage changes and Stark shift captured in the difference spectra. Contributions associated with structural dispersion of adsorption sites on the (111) textured, but nonetheless polycrystalline, Cu thin film, relative to Cu(111), may also contribute to the difference in the observed Stark shift. Previous transient measurements on Cu(111) show that the  $\text{SO}_4^{2-}$  coverage and associated Stark shift are established quickly relative to the formation of the  $\sqrt{3} \times \sqrt{7}$   $R19^\circ$  mixed  $\text{SO}_4^{2-}$ – $\text{H}_3\text{O}^+$ / $\text{H}_2\text{O}$  adlayer, indicating that extended in-plane ordering is a second-order effect relative to  $\text{SO}_4^{2-}$  binding to (111) surface segments.<sup>26,57,58</sup> An additional source of dispersion between the experiments is the pH, 0.1 mol/L  $\text{H}_2\text{SO}_4$  (SEIRAS) versus 0.005 mol/L  $\text{H}_2\text{SO}_4$  (IRRAS), which may alter the degree of protonation in the adsorbed sulfate layer, i.e.,  $\text{SO}_4^{2-}$ / $\text{HSO}_4^-$ . To explore this question, the SEIRAS experiment was repeated using deuterated reagents, and the potential-dependent spectra from one of two experiments are summarized in Figure S3b. As shown in Figure S4, the Stark shift ( $\approx 44 \pm 3.3 \text{ cm}^{-1} \text{ V}^{-1}$ ) over the 0.25 V window was slightly altered and the nominal peak positions shifted  $\approx 6 \text{ cm}^{-1}$ ; however, after correcting for the different reference state,  $-0.8$  versus  $-0.85 \text{ V}_{\text{SSE}}$  for the deuterated versus conventional experiment, the difference falls within the 4  $\text{cm}^{-1}$  measurement uncertainty, indicating that the  $\text{SO}_4^{2-}$ , not  $\text{HSO}_4^-$ , accounts for the dominant 1220–1240  $\text{cm}^{-1}$  band.

In contrast to the  $\approx 1215 \text{ cm}^{-1}$  band, no Stark shift was evident for the weaker 1114  $\text{cm}^{-1}$  band (band 3, Figure 3c). Repetition of the potential difference study of Figure 3 performed with 88  $\mu\text{mol/L}$  PEG in the electrolyte revealed a negligible impact on  $\text{SO}_4^{2-}$  spectra (Figure S4). Possible overlap exists between the C–O–C PEG backbone modes and the  $\text{SO}_4^{2-}$  band; however, the complete set of measurements, *vide infra*, indicate either minimal interaction between solvated PEG and adsorbed  $\text{SO}_4^{2-}$  or at least negligible potential dependence for whatever limited amount of PEG is co-adsorbed.

SEIRAS and IRRAS are sensitive to vibrational modes that have a significant transition dipole component aligned with the local surface normal, with the intensity proportional to surface coverage and the square of the transition dipole moment. In principle, adsorption of  $\text{SO}_4^{2-}$  or  $\text{HSO}_4^-$  may occur via one, two, or three of the oxygen atoms, with the energy and intensity of the vibrational modes of the respective adsorbed species being perturbed by the different symmetries. Table S1 provides a summary of spectral assignments for solvated sulfate species derived from ATR measurements of various electrolytes performed using the Si prism covered with its native oxide (Figures S5–S9). The results are in good agreement with literature results obtained in a transmission geometry.<sup>61</sup> For 0.1 mol/L  $\text{H}_2\text{SO}_4$ , dissociation of the diprotic acid ( $\text{p}K_a = 1.9$ ) is incomplete and the electrolyte contains 0.11 mol/L  $\text{H}_3\text{O}^+$ , 0.09 mol/L  $\text{HSO}_4^-$ , and 0.01 mol/L  $\text{SO}_4^{2-}$ . Accordingly,  $\text{HSO}_4^-$  might be expected to be the dominant adsorbed anion. However, *in situ* SERS studies of Cu in 1 mol/L  $\text{H}_2\text{SO}_4$  indicate that  $\text{SO}_4^{2-}$  is the adsorbed species, evident by a large shift and substantial broadening of the totally symmetric (Raman-active, IR-forbidden)  $\text{SO}_4^{2-}$  vibrational frequency from 982  $\text{cm}^{-1}$  for the dissolved species to 967  $\text{cm}^{-1}$  for the anion adsorbed on the roughened Cu surface.<sup>62,63</sup> The tetrahedral ( $T_d$ ) symmetry of free  $\text{SO}_4^{2-}$  is lowered by adsorption to either  $C_{3v}$  or  $C_{2v}$  with three or four active

bands, respectively.<sup>57,58,61</sup> The nominally IR-forbidden 967  $\text{cm}^{-1}$  band is also evident in the SEIRAS sulfate displacement spectra in Figure 3e congruent with the decreased symmetry accompanying its adsorption. As with the  $\approx 1215 \text{ cm}^{-1}$  SEIRAS band (Figure 3b), the 967  $\text{cm}^{-1}$  Raman peak was insensitive to isotope  $\text{H}_2\text{O}$ – $\text{D}_2\text{O}$  exchange, again pointing to adsorbed  $\text{SO}_4^{2-}$ .<sup>62</sup> Deconvolution of STM images of  $\text{SO}_4^{2-}$  adsorption on Cu(111) obtained at high tunneling conductance was used to infer a  $C_{2v}$  configuration with bridging coordination via two oxygen atoms.<sup>26,57,58</sup> However, more recent work on  $\sqrt{3} \times \sqrt{7}$   $R19^\circ$  mixed  $\text{SO}_4^{2-}$ – $\text{H}_3\text{O}^+$ / $\text{H}_2\text{O}$  adlayers formed on other close packed (111) fcc surfaces, namely, Pt, Ir, Pd, Rh, Au, as well as (0001) hexagonal close-packed Ru, favors the  $C_{3v}$  assignment.<sup>64–66</sup> Common to these isostructural anion–water adlayers on close packed metal surfaces is an intense IRRAS band between 1150 and 1310  $\text{cm}^{-1}$  and a weaker band near 950  $\text{cm}^{-1}$ . Density functional theory (DFT) calculations for Pt(111) in sulfuric acid provide an explanation for the energy, intensity, and positive Stark shift of the strong 1200–1250  $\text{cm}^{-1}$  band consistent with adsorbed  $\text{SO}_4^{2-}$ .<sup>67,68</sup> The intense band is ascribed to the large dynamic dipole moment and favorable alignment of the uncoordinated  $\nu(\text{S–O})$  stretching mode of  $\text{SO}_4^{2-}$  bound to the surface by the other three oxygen atoms.<sup>67–69</sup> The weaker band near 950  $\text{cm}^{-1}$  corresponds to the infrared-inactive symmetric  $\nu(\text{S–O})$  stretching mode of  $\text{SO}_4^{2-}$  that becomes active due to symmetry reduction that accompanies adsorption. The spectral range for the 950  $\text{cm}^{-1}$  band was only sampled in a subset of measurements, although the band is clearly present in the  $\text{SO}_4^{2-}$  displacement spectra (i.e., Figure 3e). The weaker 1114  $\text{cm}^{-1}$  band that decreases with potential in Figure 3a is attributed to the loss, or conversion, of physisorbed  $\text{SO}_4^{2-}$ . The feature is also evident in the complementary deuterated experiment shown in Figure S3b consistent with the triply degenerate  $\nu(\text{S–O})$  stretching mode for solvated  $\text{SO}_4^{2-}$  (Table S1).

**$\text{SO}_4^{2-}$  Displacement by  $\text{Cl}^-$ .** The halides  $\text{Cl}^-$ ,  $\text{Br}^-$ , and  $\text{I}^-$  adsorb strongly on group IB metal surfaces and, depending upon the potential, form high-coverage ordered phases on low-index surfaces, as revealed by STM and surface X-ray diffraction.<sup>21–31</sup> As shown in Figure 4, the addition of 1 mmol/L  $\text{Cl}^-$  to 0.1 mol/L  $\text{H}_2\text{SO}_4$  results in rapid displacement of  $\text{SO}_4^{2-}$  from the Cu surface held at  $-0.65 \text{ V}_{\text{SSE}}$ , as evident by the negative bands centered at 1215 and 1115  $\text{cm}^{-1}$  (and 965  $\text{cm}^{-1}$ , as shown in Figure 3e). Displacement of  $\text{SO}_4^{2-}$  by  $\text{Cl}^-$  was also reported in prior Raman studies.<sup>36,60</sup> Importantly, the SEIRAS images reveal that the change in adsorbed anion is accompanied by significant time-dependent perturbation and rearrangement of the interfacial water structure, as shown by the distinct changes in the  $\delta(\text{HOH})$  bending ( $\approx 1600 \text{ cm}^{-1}$ ) and  $\nu(\text{OH})$  stretching modes (3000–3600  $\text{cm}^{-1}$ ). As seen in Figure 4 following initial halide injection (+0 min), negative  $\nu(\text{OH})$  peaks, including subtle changes in the hydronium modes, are associated with the displaced  $\text{SO}_4^{2-}$ – $\text{H}_5\text{O}_2^+$  adlayer, while positive peaks reflect the restructured hydration layer that develops adjacent to the adsorbed halide. Specifically, the increase at 1625  $\text{cm}^{-1}$  suggests enhanced alignment of the  $\delta(\text{HOH})$  water mode adjacent to the halide layer, while the decrease at 1663  $\text{cm}^{-1}$  is due to disruption of the  $\text{H}_5\text{O}_2^+$  species that accompanies desorption of the  $\text{SO}_4^{2-}$ – $\text{H}_5\text{O}_2^+$  adlayer.<sup>70–72</sup> At the same time, the slight rise in the broad background intensity near 1750  $\text{cm}^{-1}$  is congruent with a slight increase of hydronium (Figures S7–S9) that may serve to screen the negative halide charge. At higher wavenumber,

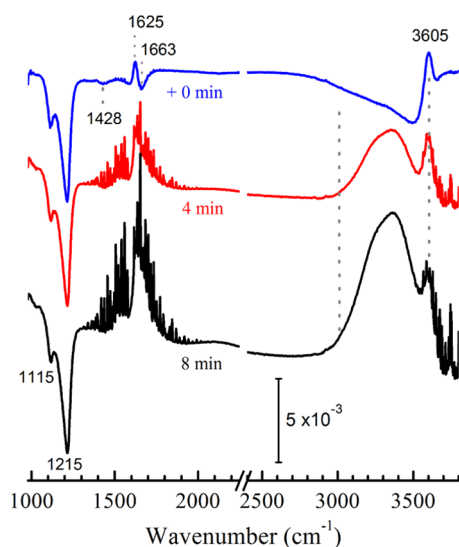


**Figure 4.** SEIRAS titration spectra at  $-0.65 V_{\text{SSE}}$  revealing displacement of  $\text{SO}_4^{2-}\text{-H}_3\text{O}^+/\text{H}_2\text{O}$  (negative peaks at 1115 and 1215  $\text{cm}^{-1}$ ) by  $\text{Cl}^-$  adsorption and rearrangement of the adjacent water structure (1600–1670 and 3000–3600  $\text{cm}^{-1}$ ) in 1 mmol/L NaCl + 0.1 mol/L  $\text{H}_2\text{SO}_4$ . The narrow non-hydrogen-bonded water at the 3600  $\text{cm}^{-1}$  band develops rapidly with the formation of the ordered  $\text{Cl}^-$  adlayer, while the hydrogen-bonded water network evolves more slowly congruent with mesoscale coarsening of the halide-covered surface. The noise artifacts in the 4 and 8 min spectra are associated with atmospheric water contamination of the spectrometer's optical path.

the  $\nu(\text{OH})$  decrease between 2750 and 3500  $\text{cm}^{-1}$  manifests the displacement and desorption of the water associated with the  $\text{SO}_4^{2-}$  adlayer along with changes in the hydronium continuum, while the more distinct and narrow increase at 3605  $\text{cm}^{-1}$  is ascribed to the formation of non-hydrogen-bonded water.<sup>52,54,55,73,74</sup> Two additional subtle bands, the minor decrease at 1430  $\text{cm}^{-1}$  and an increase near 1518  $\text{cm}^{-1}$ , are common to the difference spectra collected immediately after  $\text{Cl}^-$  titration. The inflections overlap those seen in difference spectra between acids and water (Figures S7–S9) and, according to recent theory, are ascribed to proton shuttling that involves a close coupling between bending and stretching modes.<sup>74,75</sup> The changes convolve the loss of hydronium associated with the displaced  $\text{SO}_4^{2-} + \text{H}_3\text{O}^+$  adlayer with the evolution of screening charge adjacent to the adsorbed  $\text{Cl}^-$  adlayer.

In the first approximation, disruption of the hydrogen-bonded network by halide adsorption is analogous to that associated with the solvation shell of free  $\text{Cl}^-$ .<sup>76</sup> ATR measurements of concentrated NaCl–water electrolytes clearly reveal disruptions of the hydrogen bond network of water, as shown in Figure S10. Due to surface enhancement effects, the 3600  $\text{cm}^{-1}$  mode for the  $\text{Cl}^-$  adlayer on Cu in Figure 4 greatly exceeds the bulk signal associated with the additional 1 mmol/L NaCl. Polarization provided by surface-bound  $\text{Cl}^-$  might be expected to draw dangling hydrogen of the free OH, although an alternative conformation might have the water molecules straddling the halide or aligned with nearest-neighbor halide species such that the  $\text{H}_2\text{O}$  quadrupole is aligned to the surface normal. The first non-hydrogen-bonded configuration can be compared to dangling  $\nu(\text{OH})$  stretch associated with the broken symmetry of the air–water interface.<sup>52,54,55</sup> The red shift to lower vibrational energy, from 3700  $\text{cm}^{-1}$  for simple

$\nu(\text{OH})$  to 3600  $\text{cm}^{-1}$ , reflects the nature of the charge–dipole interaction between  $\nu(\text{OH})$  and  $\text{Cl}^-$ . Importantly, a recent low-energy electron diffraction (LEED)-IV and DFT study of  $\text{H}_2\text{O}$  adsorption on Cu(100)  $c(2 \times 2)\text{Cl}^-$  indicates the formation of a weakly bound water bilayer with 50% of the first water layer H facing the  $\text{Cl}^-$  adlayer congruent with the present results.<sup>77</sup> In the case of another coinage metal surface, that of Au, a similarly narrow  $\approx 50 \text{ cm}^{-1}$  full width at half-maximum peak located between 3610 and 3582  $\text{cm}^{-1}$  has been reported to accompany halide adsorption from 1 mmol/L KX ( $X = \text{Cl}^-, \text{Br}^-, \text{or } \text{I}^-$ ) electrolyte.<sup>78</sup> A slight dependence on the cation,  $\text{Li}^+$  versus  $\text{K}^+$  was observed, while in the present experiments, electrolyte screening of negative halide charge is provided by  $\text{H}_3\text{O}^+$ . More recently, an SFG study of water–Au interactions in 1 mol/L  $\text{HClO}_4$  has revealed a free  $\nu(\text{OH})$  band at 3680  $\text{cm}^{-1}$ , whose intensity reaches a maximum near the pzc.<sup>79</sup> As the static dipole moment bisects the HOH molecule, it was argued that as the negative charge on Au increases further, neither OH bond will be perpendicular to the metal surface; rather, a balance between orientation and density effects will ensue. In a related vein, beyond the strong 3669  $\text{cm}^{-1}$  band of free OH band, SFG studies of the immiscible water/ $\text{CCl}_4$  interface reveal an additional small peak at 3600  $\text{cm}^{-1}$ , which was assigned to weakly bound monomeric water with both H facing the  $\text{CCl}_4$  phase.<sup>54,73</sup> Summarizing, the increase in non-hydrogen-bonded water indicates the development of a more hydrophobic interface congruent with disruption of the water structure that underlies the distinction between hydrophobic versus hydrophilic interfaces.<sup>52,54,55,80–82</sup>

Sequential SEIRAS spectra collected following  $\text{Cl}^-$  titration reveal a significant time dependence of the water modes as shown in Figure 4 (and Figure S11). Following halide addition, the ordered (“icelike” or tetrahedral water)  $\nu(\text{OH})$  modes around 3200  $\text{cm}^{-1}$  and disordered (“liquid” or lower coordination water)  $\nu(\text{OH})$  modes at 3400  $\text{cm}^{-1}$  increase on a time scale of minutes. Recent literature exploring the structural specificity of such  $\nu(\text{OH})$  assignments ascribes the blue shift to weakening of the hydrogen-bonding network as captured by coupling between stretching and bending overtones,<sup>83</sup> Furthermore, beyond neutral water, the  $\nu(\text{OH})$  bands also incorporate the Eigen ( $\approx 2800 \text{ cm}^{-1}$ ) and Zundel ( $\approx 3200 \text{ cm}^{-1}$ ) stretching modes of hydronium evident in Figure 4 (and Figure S11).<sup>73–75,83</sup> In the present work, the slow evolution of the 3000–3500  $\text{cm}^{-1}$  spectral band, over 8 min, following  $\text{Cl}^-$  addition is most likely correlated to coarsening of the freshly formed, ordered  $\text{Cl}^-$  domains and mesoscopic step structure that impact long-range ordering in the adjacent hydration layer.<sup>21–24,28–30</sup> Similar time-dependent microstructural effects on SEIRAS water spectra have been noted for sulfate adsorption on Au.<sup>72,84</sup>

The properties of bulk water are strongly influenced by hydrogen bonding between neighboring molecules, while solutes and interfaces disrupt the network to some extent.<sup>85,86</sup> At neat water–air interfaces, non-hydrogen-bonded, free OH groups protrude into the atmosphere.<sup>54,55</sup> The hydration shell around nonpolar molecular solutes is similarly characterized by the formation of dangling OH bonds, but with the vibrational energy red-shifted relative to that at the water–air interface due to the local electric field.<sup>80</sup> For example, the narrow, high-frequency  $\nu(\text{OH})$  band at 3700  $\text{cm}^{-1}$  observed at the water–air interface downshifts to 3674  $\text{cm}^{-1}$  at the water–oil interface while for neopentanol and related alkane groups in

water, the peak shifts to  $3661 \pm 2 \text{ cm}^{-1}$  and for H- $\pi$  aromatic ring interactions shifts to  $3600 \text{ cm}^{-1}$  have been reported.<sup>80,81,87</sup> Accordingly, the band at  $3600 \text{ cm}^{-1}$  in Figure 4 is assigned to an increase in non-hydrogen-bonded water,  $\nu(\text{OH})$ , either as the dipole or quadrupole, induced by the negative charge of the  $\text{Cl}^-$ -saturated surface. The increase in non-hydrogen-bonded water at  $3600 \text{ cm}^{-1}$  is accompanied by a similar increase in the  $\delta(\text{HOH})$  scissoring mode at  $1625 \text{ cm}^{-1}$ , and perhaps a slight increase in the hydronium continuum. With electrode aging, the envelope of hydrogen-bonded water reforms and strengthens as the domain size of the templating ordered  $\text{Cl}^-$  adlayer coarsens. The  $\text{SO}_4^{2-}$  displacement experiments were repeated multiple times, e.g., Figure S11, with fresh electrodes to verify that  $\text{Cl}^-$  titration and adsorption yield an increase in the  $3600 \text{ cm}^{-1}$  non-hydrogen  $\nu(\text{OH})$  stretch and the  $1625 \text{ cm}^{-1}$   $\delta(\text{HOH})$  bending mode. Similar effects were also noted for  $\text{Cl}^-$  displacement of  $\text{SO}_4^{2-} + \text{D}_5\text{O}_2^+$  in deuterated electrolyte, as shown in Figure S11b. The  $\nu(\text{OH})$  peak at  $2659 \text{ cm}^{-1}$  is ascribed to non-hydrogen-bonded water, while the overlaps between the increase in  $\delta(\text{DOD})$  with the loss of  $\text{SO}_4^{2-}$  is evident. Most importantly, the development of non-hydrogen-bonded water and its association with hydrophobic interfaces have important implications for the co-adsorption of molecular species on halide-covered surfaces.

Recently, LEED and X-ray surface scattering have been applied to examine  $\text{Cl}^-$  adlayers on (111) and (100) Cu surfaces.<sup>28–31,77</sup> Modeling scattering from a Cu(100)  $c(2 \times 2)$   $\text{Cl}^-$  surface indicates the halide adlayer templates lateral ordering of the adjacent water and hydronium species.<sup>28,30,77</sup> For acid solutions, hydronium is thought to preferentially occupy hollow sites in the anionic layer, while the inner (anionic,  $\text{Cl}^-$ ) and outer (cationic,  $\text{H}_3\text{O}^+$ ) components of the Helmholtz layer compete for water to form their respective solvation shells.<sup>28</sup> Accordingly, the potential-dependent order-disorder phase transitions associated with halide adlayers provides a useful avenue to probe the connection between adsorbed anions and the neighboring water structure. As shown in Figure 5, SEIRAS images following a potential step from  $-0.65$  to  $-0.8 \text{ V}_{\text{SSE}}$  reveal a decrease in the  $\delta(\text{HOH})$  and non-hydrogen-bonded  $\nu(\text{OH})$  water bands due to a combination of partial desorption and disordering of the  $\text{Cl}^-$  adlayer. The absence of any sign of sulfate adsorption indicates that the

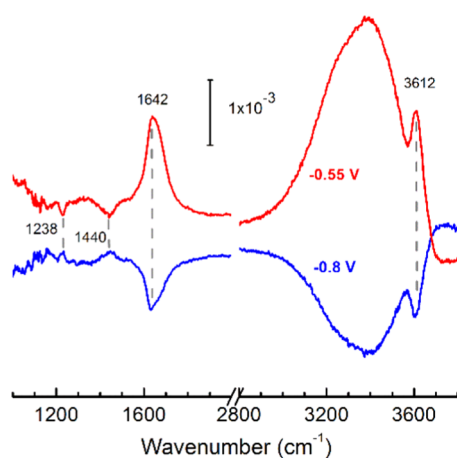


**Figure 5.** SEIRAS images, referenced to  $-0.65 \text{ V}_{\text{SSE}}$ , show the impact of potential-dependent phase transitions in the  $\text{Cl}^-$  adlayer on the adjacent water layer in  $1 \text{ mmol/L NaCl} + 0.1 \text{ mol/L H}_2\text{SO}_4$ .

coverage of the disordered  $\text{Cl}^-$  layer is still significant enough to prevent sulfate adsorption despite the latter being 100-fold greater in concentration. A similar result was seen in a SERS and surface X-ray diffraction study.<sup>30,60</sup> When the potential is stepped to a more positive value of  $-0.55 \text{ V}_{\text{SSE}}$  the free OH and other water vibrational modes are intensified relative to the values observed at  $-0.65 \text{ V}_{\text{SSE}}$ . The potential dependence of the  $3000\text{--}3500 \text{ cm}^{-1}$   $\nu(\text{OH})$  hydrogen-bonded water envelope tracks that of the non-hydrogen-bonded water near  $3612 \text{ cm}^{-1}$  congruent with templating between a compact ordered halide adlayer and neighboring water structure. The minor changes at  $1238$  and  $1440 \text{ cm}^{-1}$  are ascribed to changes in the hydronium shuttling and umbrella modes.<sup>75</sup>

**PEG Adsorption on  $\text{Cl}^-$ -Terminated Cu.** PEG adsorption was examined both in the presence and absence of  $\text{Cl}^-$ . Accordingly, following the  $\text{SO}_4^{2-}$  adsorption experiments,  $1 \text{ mmol/L Cl}^-$  was added to the  $0.1 \text{ mol/L H}_2\text{SO}_4$  electrolyte and displacement of the  $\text{SO}_4^{2-}\text{--H}_3\text{O}^+/\text{H}_2\text{O}$  adlayer and the development of the narrow  $\delta(\text{HOH})$  and  $\nu(\text{OH})$  water modes due to  $\text{Cl}^-$  adsorption at  $-0.65 \text{ V}_{\text{SSE}}$  was verified, as shown by the spectrum in Figure 6. This was followed by the addition of

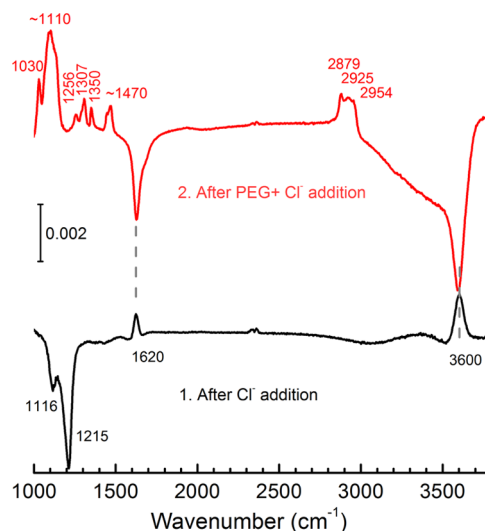


**Figure 6.** SEIRAS difference spectra collected at  $-0.65 \text{ V}_{\text{SSE}}$  after  $\text{Cl}^-$  titration (black) ( $1 \text{ mmol/L NaCl} + 0.1 \text{ mol/L H}_2\text{SO}_4$ ), followed by the addition of PEG (red) ( $88 \mu\text{mol/L PEG} + 1 \text{ mmol/L NaCl} + 0.1 \text{ mol/L H}_2\text{SO}_4$ ). The disruption of water modes by  $\text{Cl}^-$  adsorption facilitates subsequent co-adsorption of PEG, wherein water is displaced by the hydrophobic segments while the ethereal oxygen sites are available for hydrogen bonding.

$88 \mu\text{mol/L PEG}$  ( $M_w = 3400 \text{ g/mol}$ ) to the cell, and the difference spectrum reveals PEG adsorption with multiple peaks for the different polymer modes. The large multi-component peak with a maximum intensity near  $1100 \text{ cm}^{-1}$  and the narrow adjacent peak at  $1030 \text{ cm}^{-1}$  are ascribed to combinations of C-O and C-C polyether backbone vibrations and  $\text{CH}_2$  rocking modes. Four smaller peaks between  $1200$  and  $1500 \text{ cm}^{-1}$  are associated with the  $\text{CH}_2$  twist,  $\text{CH}_2$  wag, and  $\text{CH}_2$  scissor modes, while the  $\text{CH}_2$  stretches are evident between  $2850$  and  $3000 \text{ cm}^{-1}$ .<sup>88–90</sup> PEG adsorption is accompanied by a marked decrease in the water modes, including the narrow non-hydrogen-bonded  $\nu(\text{OH})$  stretch at  $3600 \text{ cm}^{-1}$  and the  $\delta(\text{HOH})$  bending mode at  $1620 \text{ cm}^{-1}$ , both formerly associated with the saturated  $\text{Cl}^-$  layer, and the broad loss of intensity between  $3000$  and  $3500$

$\text{cm}^{-1}$  for hydrogen-bonded  $\nu(\text{OH})$  water modes. The negative  $\delta(\text{HOH})$  peak has a notable shoulder at higher wavenumber, near  $1660 \text{ cm}^{-1}$ , which in combination with the sloping background beneath the  $\text{CH}_2$  stretching modes,  $2850\text{--}3000 \text{ cm}^{-1}$ , is attributed to a decrease or rearrangement of hydronium at the interface. In brief, PEG adsorption disrupts and displaces the hydration layer adjacent to the halide adlayer as its hydrophobic character favors polyether adsorption over non-hydrogen-bonded water. The hydrophobic  $-\text{CH}_2-\text{CH}_2-$  segments are drawn to the  $\text{Cl}^-$  adlayer, while the lone pair electrons of the intervening ether  $-\text{O}-$  contribute to the formation of the hydrogen bond network with the adjacent solvent such that the free energy of the  $\text{Cu}-\text{Cl}^-$ -PEG layered interface is minimized.

Further insight into the structure of the adsorbed polyether layer is obtained by comparison to spectra for the dissolved and crystalline forms. Spectra for crystalline PEG powder were collected using a KBr mull in transmission mode, while a series of PEG-water and PEG- $0.1 \text{ mol/L H}_2\text{SO}_4$  solutions were examined by ATR using the Si prism with its native oxide film. Representative results for crystalline and solvated PEG ( $M_w = 3400$ ) along with the deuterated variants are shown in Figures S12–S17. Peak assignments are based on prior literature that include an assessment of the dichroic nature of textured samples, as summarized in Tables S2 and S3.<sup>88,89,91–93</sup>

The concentration dependence of the spectral features of solvated PEG was used to quantify the surface enhancement associated with spectra for PEG adsorption on the  $\text{Cl}^-$ -covered Cu films. The difference spectra for PEG dissolved in water are shown in Figure S12, and the magnitude of selected peaks are summarized in Figure S13. Without surface enhancement from the Cu film, solvated PEG does not contribute significantly to the ATR spectra for the  $88 \mu\text{mol/L}$  PEG solution. The enhanced signal associated with chemisorption on the  $\text{Cl}^-$ -covered Cu surface ranges from a 150-fold increase in absorbance for the  $1093 \text{ cm}^{-1}$  C–C–O modes to a 450-fold increase for the  $2885 \text{ cm}^{-1}$  methylene stretch modes, as evident in Figure S13. The variation between individual bands reflects the conformation of the adsorbed versus solvated polymer, as detailed below. The spectra in Figure S12 also reveal the impact of solvated PEG on the water structure itself. Specifically, for additions of up to  $16 \text{ mmol/L}$  PEG, a decrease in the non-hydrogen-bonded  $\nu(\text{OH})$  water is evident due to the hydrogen-bonding sites provided by the polyether.

Examination of the C–C–O– backbone and  $\text{CH}_2$  modes of the adsorbed PEG- $\text{Cl}^-$  suppressor layer reveals several important differences relative to solvated PEG. The intensity ratio of the C–C–O– envelope,  $1000\text{--}1200 \text{ cm}^{-1}$  in Figure 7a (and Figure S18a), to the methylene bands,  $2700\text{--}3100 \text{ cm}^{-1}$  in Figure 7b (and Figure S18b), decreases from 4.75 for the solvated polymer to 2.5 for the adsorbed layer. The anisotropy reflects the structure and orientation of the adsorbed PEG layer convolved with the IR selection rules, SEIRAS only being sensitive to components of dipole transitions that are perpendicular to the local surface normal. The change in the ratio of the C–C–O– envelope to the  $\text{CH}_2$  modes implies a net preferential arrangement of the  $\text{CH}_2$  modes along the local surface normal and/or preferential arrangement of the C–C–O within the surface plane. Other spectral features of interest are the increased intensity of the  $1030 \text{ cm}^{-1}$  band, changes in the component contributions to the  $\approx 1095 \text{ cm}^{-1}$  C–C–O– and methylene envelope, and variations in the other  $\text{CH}_2$  modes as indicated in Figure 7c.

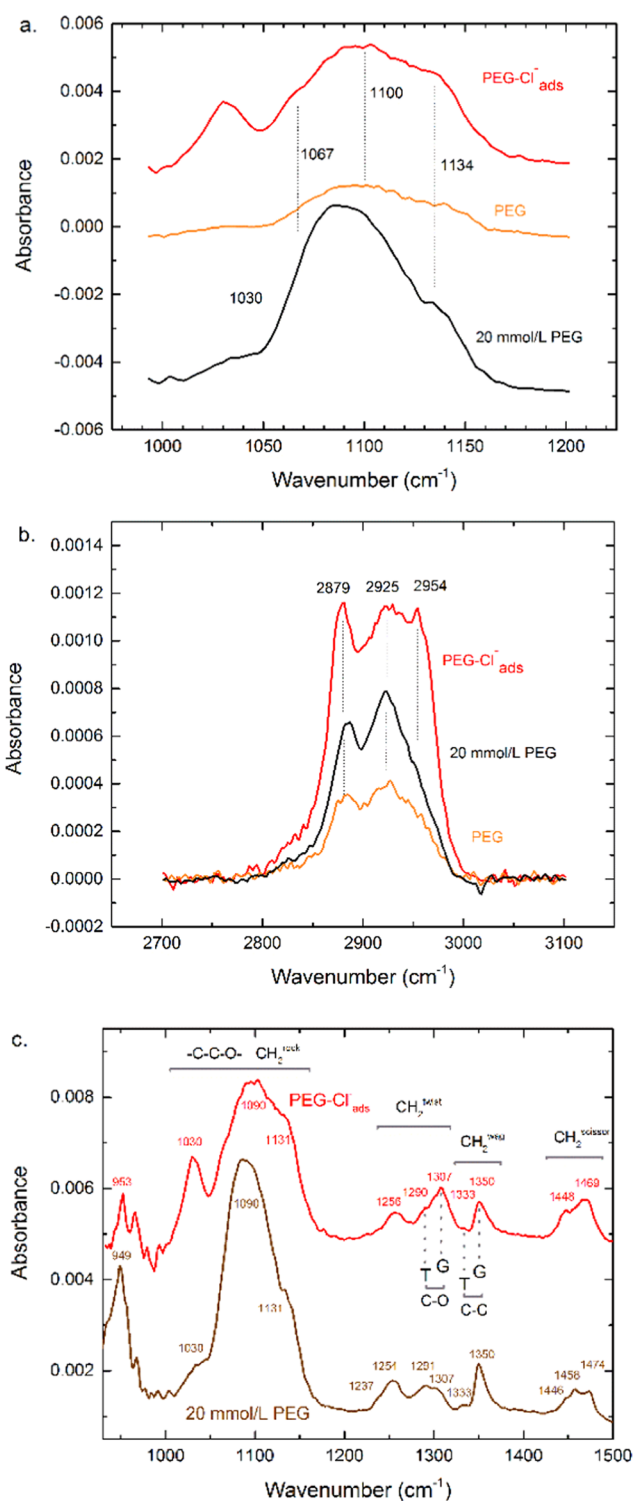


**Figure 7.** SEIRAS spectra for co-adsorbed PEG- $\text{Cl}^-$  ( $88 \mu\text{mol/L}$  PEG) and weakly adsorbed PEG ( $88 \mu\text{mol/L}$  PEG) compared to solvated PEG ( $20 \text{ mmol/L}$  PEG). The shape and relative magnitude (see text) of the (a)  $-\text{C}-\text{C}-\text{O}-$  envelope and (b)  $\text{CH}_2$  stretch region reflect the anisotropy associated with PEG adsorption on the  $\text{Cl}^-$ -covered Cu surface. (c) The PEG- $\text{Cl}^-$  layer exhibits increased intensity of the  $1030 \text{ cm}^{-1}$  C–C–O–,  $\text{CH}_2^{\text{rock}}$ , and  $1307 \text{ cm}^{-1}$   $\text{CH}_2^{\text{twist}}$  modes due to an increase in the percentage of gauche (G) C–O–C segments associated with deviation of the adsorbed molecules from the dominant helical arrangement of solvated PEG. Deconvolutions of the spectral envelope in (a) and (b) are provided in Figure S18.

A close inspection of the multicomponent peak envelope centered near  $1100\text{ cm}^{-1}$  in Figure 7a (the deconvolved components shown in Figure S18a and listed in Table S4) reveals that the ratio of  $1100/1067\text{ cm}^{-1}$  and  $1100/1134\text{ cm}^{-1}$  components for the adsorbed polymer are significantly reduced compared to solvated PEG, while the opposite is true for the adjacent band at  $1030\text{ cm}^{-1}$ . Previous polarized infrared spectra for highly oriented crystalline PEG specimens (summarized in Table S3) provide insight into these differences,<sup>92,93</sup> when the main helical axis of PEG lies within the surface plane, the modes exhibiting perpendicular dichroism are favored while the opposite is true for parallel dichroism. Accordingly, with reference to spectra for oriented crystalline PEG and isotropic solvated PEG, the perpendicular modes  $\nu(\text{C}-\text{O}-\text{C}) + \tau(\text{CH}_2)$  at  $1060\text{ cm}^{-1}$ ,  $\nu(\text{C}-\text{C}) + \nu(\text{C}-\text{O}-\text{C})$  at  $1147\text{ cm}^{-1}$ , and  $\nu(\text{C}-\text{O}-\text{C})$  at  $1116\text{ cm}^{-1}$  of the adsorbed PEG layer are favored over the parallel  $\nu(\text{C}-\text{O}-\text{C})$  mode at  $1103\text{ cm}^{-1}$ . Likewise, as shown in Figure 7b (the deconvolved components shown in Figure S18b and listed in Table S4), the intensities of the components of the methylene envelope, also affected by dichroism, show an increase in the perpendicular component of the antisymmetric stretch at  $2950\text{ cm}^{-1}$  congruent with the assumption that PEG lies in the plane of the  $\text{Cl}^-$ -covered Cu surface. The same arguments apply to the relative intensity of the rock, twist, wag, and scissor modes, as detailed below.

In the solid state, crystalline PEG/PEO adopts a helical form with rotation about the C–C bond in the O–C–C–O sequence in the gauche (G) ( $\pm 60^\circ$  about the C–C backbone bond axis) conformation, while the C–O–C bond maintains a trans (T) ( $180^\circ$  rotation) configuration.<sup>89,92,93</sup> The trans-gauche-trans (T–G–T) O–C–C–O helical form has the hydrogen in  $\text{CH}_2$  pointing outward, while the ether oxygen points inward toward the helical axis. When dissolved in water, hydration interactions between the polar ether, nonpolar alkyl groups, and surrounding water stabilize the T–G–T conformation with hydrogen bonding between ether O and water.<sup>88–91</sup> The situation is optimal when the C–C bond is G such that the  $0.29\text{ nm}$  spacing between neighboring ether O atoms is close to the  $0.285\text{ nm}$  O–O distance in liquid water. Defects and variations in the water-stabilized helical conformations are conferred by  $\pm\text{G}$  rotation about the C–C bond, while deviations from the T conformation about the C–O axis provide important structural flexibility. Interestingly, for higher PEG concentrations in water, chain interactions are dominated by hydration forces, and the formation of flexible plates one molecule in thickness has been suggested.<sup>91</sup> Adsorption is associated with additional interactions due to the double-layer electric field and wetting forces that can influence polymer assembly on the  $\text{Cl}^-$ -covered Cu surface. In principle, this can include configurations that deviate substantially from the helical conformation that, among other variants, could include arrangements where the polar ether and nonpolar alkyl groups are biased to opposite sides of the molecule, whereby the amphiphilic character is expressed and stabilized by the metal–electrolyte interface.<sup>90</sup> Indeed, the use of electrode polarization to induce conformation bias has been recently demonstrated for crown ether moieties adsorbed on graphene surfaces.<sup>94</sup> In a similar fashion, the impact of co-adsorption of cationic species has also been explored.<sup>47,49,94</sup>

The  $\text{CH}_2$  modes evident in Figure 7c include the antisymmetric  $\text{CH}_2$  twist at  $1256\text{ cm}^{-1}$ , the symmetric  $\text{CH}_2$  twist at  $1292\text{--}1307\text{ cm}^{-1}$ , the antisymmetric  $\text{CH}_2$  wag at

$1333\text{--}1350\text{ cm}^{-1}$ , and the  $\text{CH}_2$  scissor at  $1446\text{--}1474\text{ cm}^{-1}$ . The  $\text{CH}_2$  twist and wag modes are diagnostic of the G/T conformation around the C–O and C–C bonds, respectively.<sup>88,89</sup> The  $\text{CH}_2$  twist modes at  $1292$  and  $1307\text{ cm}^{-1}$  correspond to T and G conformations about the C–O bond, while  $\text{CH}_2$  wag modes at  $1325$  and  $1350\text{ cm}^{-1}$  correspond to the T and G states about the alkyl C–C bond, respectively. The spectra in Figure 7c show that the G form of the asymmetric  $\text{CH}_2$  wag at  $1350\text{ cm}^{-1}$  dominates the T band at  $1325\text{ cm}^{-1}$  for both the PEG– $\text{Cl}^-$  layer and the solvated polymer. This is in good agreement with literature results for short- ( $M_w = 600\text{ g/mol}$ ) and long-chain ( $M_w = 2000\text{ g/mol}$ ) PEG dissolved in water, indicating that the water-stabilized G conformation about the C–C bond of fully solvated species is maintained in the adsorbed PEG– $\text{Cl}^-$  layer.<sup>88</sup> In contrast, the conformation about the C–O bond is substantially altered by adsorption on the  $\text{Cl}^-$ -covered surface. For dissolved PEG, the  $1305\text{ cm}^{-1}$  (G) to  $1288\text{ cm}^{-1}$  (T) peak height ratio for the  $\text{CH}_2$  twist band is close to unity, consistent with prior literature results (see Figure 10 in ref 88). However, for PEG adsorbed on the  $\text{Cl}^-$ -covered surface, the  $1307\text{ cm}^{-1}$  G band is substantially greater than the  $1292\text{ cm}^{-1}$  T peak, indicating a substantial increase in the G conformation about the C–O bonds.

In addition to the increased G conformation about the C–O bonds, a survey of the literature indicates that the prominent narrow band at  $1030\text{ cm}^{-1}$ , ascribed to a combination of C–O and C–C polyether backbone and  $\text{CH}_2$  rocking modes, is not widely observed and may be taken as another important marker of PEG conformation change upon adsorption on the  $\text{Cl}^-$ -covered Cu surface. A normal coordinate analysis of the hybridized coupling between various –C–C–O– backbone modes of  $\text{CH}_3(\text{OCH}_2\text{CH}_2)_n\text{OCH}_3$  oligomers with  $n = 2, 3,$  and  $6$  suggests that the  $1030\text{ cm}^{-1}$  band is associated with either the  $x\text{TG-TG}x$  or  $x\text{GG-GG}x$  sequence (among the 72 different conformations of  $\text{CH}_3\text{O-CH}_2\text{-CH}_2\text{-O-CH}_2\text{-CH}_2\text{-OCH}_3$  examined), with the caveat that neither hydrogen bonding nor related chain–chain or chain–surface interactions were considered in the analysis.<sup>89</sup> A recent STM study of PEG adsorption on negatively charged Au revealed a monolayer film with extended winding, linear features (Figure 2f of ref 43) congruent with individual polymer chains. The surface-confined packing and meandering nature of individual PEG chains is consistent with the measured increase in G conformation about the C–O bond. The strength of the  $1030\text{ cm}^{-1}$  band, relative to that for the solvated state, indicates disruption of PEG's helical structure congruent with additional G conformation about the C–O bonds. The above features, combined with quenching of the non-hydrogen-bonded water modes associated the  $\text{Cl}^-$ -terminated surface, suggest a structural bias with  $\text{CH}_2$  groups facing the halide-covered metal, while the ethereal O forms hydrogen bonds with the adjacent solvent. Further support for this interpretation is provided by an electrospray mass spectrometry study that indicates an association between  $\text{Cl}^-$  and short-chain polyethers.<sup>95</sup> Accompanying molecular dynamics simulations suggest that the halide is coordinated with – $\text{CH}_2$ – groups of the polymer to form quasi-cyclic structures, analogous to crown ether cationic complexes but with the polarity inverted.

Performing the same SEIRAS experiment in the absence of halide (Figures 7a,b and S16–S18 and Table S4) results in a much smaller PEG signal; the intensity of the  $1000\text{--}1200\text{ cm}^{-1}$  –C–C–O– backbone and  $2750\text{--}3050\text{ cm}^{-1}$  CH stretch

envelope being 0.38 and 0.29, respectively, of that for the PEG-Cl<sup>-</sup> suppressor layer. Furthermore the shape of the -C-O-C- backbone and CH<sub>2</sub> modes have features in common with solvated species, indicating weak physisorption of the polymer.

PEG co-adsorption with Cl<sup>-</sup> was also examined using the deuterated polymer, dPEG, as summarized in Figure S17. Consistent with PEG, there is a relative attenuation of C-C-O modes polarized along the chain axis, reflecting the anisotropy associated with dPEG adsorption as a surface-confined train on the Cl<sup>-</sup>-covered Cu electrode. In the absence of Cl<sup>-</sup>, only a very weak spectrum is observed for dPEG congruent with the results for PEG alone.

**Effect of Potential.** As PEG adsorption is facilitated by the effect of Cl<sup>-</sup> on interfacial water structure, the perturbation of the underlying halide layer by its potential-dependent order-disorder phase transition was used to further probe the nature of polyether co-adsorption. Prior work on Cu(100) (and related unpublished work on Cu(110)) reveals that the Cl<sup>-</sup> order-disorder transition on the respective crystal surfaces in 1 mmol/L NaCl + 0.1 mol/L H<sub>2</sub>SO<sub>4</sub> is shifted -50 mV by the addition of PEG, indicating stabilization of the ordered Cl<sup>-</sup> phase by polyether co-adsorption.<sup>19,25,29</sup> Difference spectra following a potential step to values more positive and negative of -0.65 V<sub>SSE</sub> are shown in Figure 8 and suggest disruption of

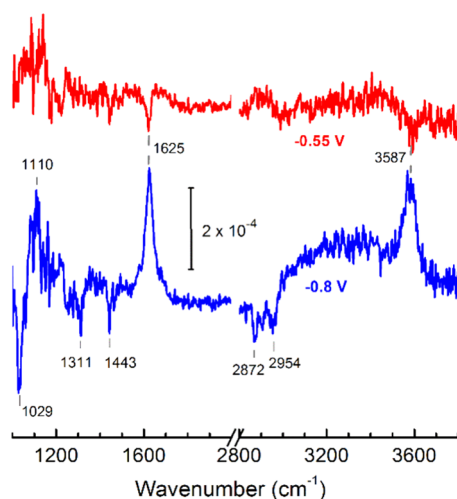


**Figure 8.** SEIRAS experiments revealing the potential dependence of the PEG-Cl<sup>-</sup> suppressor layer. Upon stepping from -0.65 to -0.8 V<sub>SSE</sub>, disruption of the polymer occurs as evident in the negative polymer bands and the complimentary increase in water and non-hydrogen-bonded water modes. In contrast, stepping from -0.65 to -0.55 V<sub>SSE</sub> leads to a loss of water modes and increase in the polymer -C-C-O- and CH<sub>2</sub> modes.

the PEG-Cl<sup>-</sup> layer at negative potentials. At more positive potentials, -0.55 V<sub>SSE</sub>, an additional increment of PEG adsorption is manifest as a slight increase of the -C-O-C- backbone band (1110 cm<sup>-1</sup>) and CH<sub>2</sub> stretch region (2800 cm<sup>-1</sup>) accompanied by a decrease in the non-hydrogen-bonded water  $\nu$ (OH) near 3600 cm<sup>-1</sup> and the  $\delta$ (HOH) at 1625 cm<sup>-1</sup>. In contrast, stepping to -0.80 V<sub>SSE</sub> leads to a loss of intensity of the PEG backbone mode at 1029 cm<sup>-1</sup>, -C-O-C- and CH<sub>2</sub> twist (G) modes near 1311 cm<sup>-1</sup>, scissor mode at 1443 cm<sup>-1</sup>, and C-H stretch modes between 2872 and 2954 cm<sup>-1</sup>. The paradoxical increase in the 1110 cm<sup>-1</sup> band may reflect reorientation and partial solvation of the

polymer backbone segments related to the loss of the 1029 cm<sup>-1</sup> mode. Partial desorption and/or rearrangement of the polymer is accompanied by an increase in the  $\delta$ (HOH) at 1625 cm<sup>-1</sup> and the non-hydrogen-bonded  $\nu$ (OH) water stretch near 3600 cm<sup>-1</sup>, along with a weaker increase in the broad envelope for hydrogen-bonded water. The changes reflect strengthening of non-hydrogen-bonded water modes on surface regions where PEG is lost from the interface. The disruption of the PEG layer at negative potential is congruent with and underlies the increase of the metal deposition rate at negative potentials evident in Figure 1 and in numerous other studies.<sup>3,5,8-17</sup> It is notable that the potential induced alterations of the water mode are only 10–20% the size of, and anticorrelated with, those observed when the experiment is performed in the presence of Cl<sup>-</sup> alone (i.e., Figure 5), which reflects the cooperative and competitive interactions between PEG, Cl<sup>-</sup> and water during co-adsorption.

**PEG Adsorption on Cu in the Absence of Cl<sup>-</sup>.** The importance of halide adsorption to polyether co-adsorption was also examined by reversing the order of additive addition, namely, PEG followed by Cl<sup>-</sup>. As in Figure 7a, Figure 9a shows detailed difference spectra collected at -0.65 V<sub>SSE</sub> after the addition of 88  $\mu$ mol/L PEG to 0.1 mol/L H<sub>2</sub>SO<sub>4</sub> revealing a small increment of PEG adsorption. The vibrational bands are significantly smaller than those obtained from the PEG layer formed in the presence of Cl<sup>-</sup>. The intensity of the 1100 cm<sup>-1</sup> multicomponent peak for the backbone C-O-C modes of PEG on Cu is 38% that observed for the PEG-Cl<sup>-</sup> layer on Cu. PEG adsorption is accompanied by a measurable but small loss of sulfate intensity near 1216 cm<sup>-1</sup>. The PEG layer formed in the absence of Cl<sup>-</sup> clearly adopts a different structure as reflected by the absence of the associated signature mode at 1030 cm<sup>-1</sup>. Similarly, the 1307 cm<sup>-1</sup> symmetric twist is greatly diminished, its intensity of similar order to the 1290 cm<sup>-1</sup> peak, indicating that the proportion of gauche C-O bonds for adsorbed PEG is significantly less than that for the PEG-Cl<sup>-</sup> layer. In fact, the 1290/1307 cm<sup>-1</sup> peak ratio is close to unity, like that reported for the fully solvated polymer.<sup>88</sup>

**Influence of Cl<sup>-</sup> Additions on PEG Adsorption.** The addition of Cl<sup>-</sup> to electrolyte already containing PEG induces significant changes, as shown in the difference spectra in Figure 9a. Displacement of the SO<sub>4</sub><sup>2-</sup> species by Cl<sup>-</sup> adsorption is evident from the negative peaks centered at 1217, 1117, and 969 cm<sup>-1</sup>, similar to its displacement observed in the absence of PEG. In the presence of PEG, subsequent Cl<sup>-</sup> adsorption is accompanied by the development of the signature peak at 1030 cm<sup>-1</sup> and an increase in the intensity at 1307 cm<sup>-1</sup> for the CH<sub>2</sub> twist, 1350 cm<sup>-1</sup> for the CH<sub>2</sub> wag, and 1447 and 1470 cm<sup>-1</sup> for the CH<sub>2</sub> scissor. The 1030 and 1307 cm<sup>-1</sup> bands reflect a significant increase in the population of C-O bonds in the gauche conformation. The increased PEG coverage associated with Cl<sup>-</sup> introduction and adsorption is also reflected in the increased intensity of the CH<sub>2</sub> stretch spectrum shown in Figure 9b and relative strengthening of the 2878 and 2954 cm<sup>-1</sup> CH<sub>2</sub> modes. Summing the methylene stretch spectra for the sequential addition of PEG and Cl<sup>-</sup> gives a favorable agreement with that obtained for the inverse order, namely, PEG adsorption on the Cl<sup>-</sup>-covered Cu surface. The related increase in the polyether backbone modes centered near 1095 cm<sup>-1</sup> in Figure 9a is partly obscured by the loss of SO<sub>4</sub><sup>2-</sup> that accompanies the halide addition. Nonetheless, the Cl<sup>-</sup>-induced increase in polyether coverage inferred from the methylene stretch band 2878–2954 cm<sup>-1</sup> for PEG and PEG-Cl<sup>-</sup>

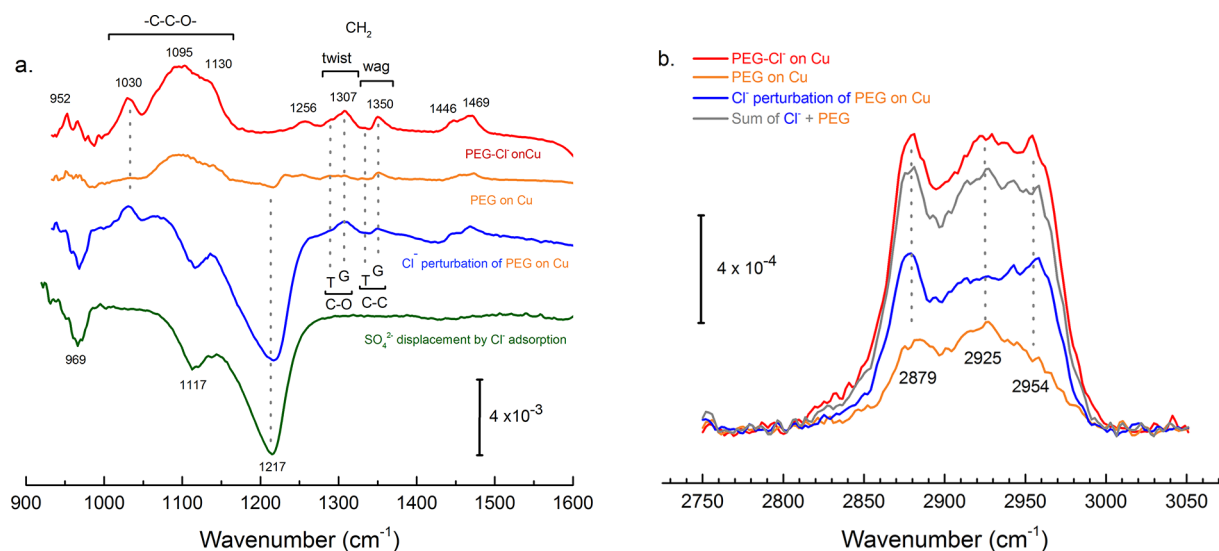


**Figure 9.** (a) C–C–O– backbone spectra based on the order of additive titration at  $-0.65 V_{SSE}$ ; PEG addition to NaCl + H<sub>2</sub>SO<sub>4</sub> (red), PEG addition to H<sub>2</sub>SO<sub>4</sub> (orange), NaCl addition to PEG + H<sub>2</sub>SO<sub>4</sub> (blue), NaCl to H<sub>2</sub>SO<sub>4</sub> (green). (b) Dependence of methylene spectra on the order of additive titration at  $-0.65 V_{SSE}$ ; PEG addition to NaCl + 0.1 mol/L H<sub>2</sub>SO<sub>4</sub> (red), PEG addition to H<sub>2</sub>SO<sub>4</sub> (orange), and NaCl addition to PEG + H<sub>2</sub>SO<sub>4</sub> (blue). The final concentrations of the respective additives in 0.1 mol/L H<sub>2</sub>SO<sub>4</sub> were 1 mmol/L NaCl and 88 μmol/L PEG.

compares favorably to the increase in the other CH<sub>2</sub> polymer modes. Examination of the complete spectral window reveals the loss of hydronium and water with the displacement of SO<sub>4</sub><sup>2-</sup> and co-adsorption of Cl<sup>-</sup> and formation of the PEG–Cl<sup>-</sup> layer (Figure S19). Within the variation observed between multiple experiments, the shape and magnitude of the linear combination of the PEG and Cl<sup>-</sup> spectra in Figure 9a compare favorably to those of the PEG–Cl<sup>-</sup> spectra. The demonstration that the final suppressor layer is essentially independent of the order of additive addition is consistent with ellipsometry measurements, which indicated that the optical thickness of the PEG–Cl<sup>-</sup> layer is independent of the order of additive addition.<sup>34</sup>

Numerous electrodeposition studies have demonstrated that Cl<sup>-</sup> is required to form an effective polyether suppressor layer for inhibiting Cu deposition reactions.<sup>3–17</sup> Comparing the PEG–Cl<sup>-</sup> layer to PEG adsorbed in the absence of Cl<sup>-</sup> indicates that the conformation(s) associated with increased intensity of the 1030 and 1307 cm<sup>-1</sup> band is associated with the formation of an effective blocking layer. The increased band intensity for co-adsorbed PEG–Cl<sup>-</sup>, versus PEG alone, reflects additional mass density and thereby a more compact overlayer. Effective packing of the nominally linear molecule on the hydrophobic Cl<sup>-</sup>-covered surface will involve kinks and in-plane loops that necessarily involve deviations from the polymer's native helical form that manifest in the increase in G conformations about the C–O bonds in the polymer backbone. At the same time, the dominant G arrangement of the C–C bonds supports effective coupling of ethereal oxygen to the hydrogen bond network in the adjacent electrolyte.

**Poloxamer and Poloxamine Adsorption on Cl<sup>-</sup>-Covered Cu.** The aspect ratio of recessed features that can be filled by superconformal copper deposition is dependent on the dynamic range available between suppressed and actively growing surfaces.<sup>3–20</sup> The search for more effective suppressors has largely focused on more complex polyethers ranging from block copolymers to star-shaped block copolymers as well as exploration of the role of fixed charges.<sup>5,15,96–102</sup> Herein, two different classes of polyethers, poloxamer and poloxamine,

have been selected to examine the role of oligomer chemistry and secondary structure in the adsorption process (see Figure 1).<sup>103–106</sup> Poly(propylene oxide) (PPO) is the largest component in both molecules. The methyl side group introduces additional hindrance to hydration that sharply increases the hydrophobic character relative to poly(ethylene oxide) (PEO). For higher-molecular-weight triblock PEO–PPO–PEO poloxamers, variations in hydration often result in the formation of a polymer brush conformation, where the central PPO segment is segregated to surfaces while the PEO termini are solvated within the aqueous phase.<sup>104</sup> Compared to PEG, hydration forces are expected to favor a more spherical conformation for the PPO core of the poloxamer of interest, PEO<sub>2</sub>PPO<sub>31</sub>PEO<sub>2</sub>. For the poloxamine, (PEO<sub>4</sub>PPO<sub>13</sub>)<sub>2</sub>N–(CH<sub>2</sub>)<sub>2</sub>N(PPO<sub>13</sub>PEO<sub>4</sub>)<sub>2</sub>, the ethylenediamine core provides additional steric constraint, while protonation of the diamine core gives rise to a fixed charge.<sup>105,106</sup> In the present work, the PEO blocks that facilitate solvation of the poloxamer and poloxamine are quite short, a 2-mer and ≈4-mer, respectively, while the hydrophobic PPO core is expected to increase the strength of polymer adsorption at hydrophobic surfaces.

For typical polymer and Cl<sup>-</sup> concentrations used for superconformal electrodeposition, inhibition of Cu deposition increases with the development of secondary structural motifs, as shown in Figure 1. SEIRAS experiments probing the co-adsorption of these polymers with Cl<sup>-</sup> reveal trends similar to that observed with PEG. As shown in Figures 10 and 11, the addition of halide at  $-0.65 V_{SSE}$  displaces the SO<sub>4</sub><sup>2-</sup>–H<sub>3</sub>O<sup>+</sup>/H<sub>2</sub>O layer and results in the development of significant non-hydrogen-bonded interfacial water (≈3600 cm<sup>-1</sup>). The subsequent addition of the poloxamer (Figure 10) or poloxamine (Figure 11) results in polyether adsorption on the hydrophobic Cl<sup>-</sup>-covered surface accompanied by a substantial decrease in both non-hydrogen-bonded and hydrogen-bonded water. For both polymers, the large multicomponent peaks at 1084 and 1088 cm<sup>-1</sup>, along with the small narrow bands at 1012 and 1014 cm<sup>-1</sup>, correspond chiefly to C–O–C backbone modes. The 1088 cm<sup>-1</sup>

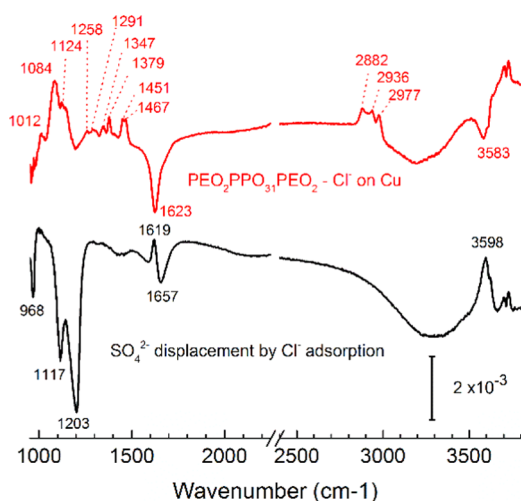


**Figure 10.** SEIRAS difference spectra at  $-0.65 V_{SSE}$  after  $Cl^-$  titration (black) (1 mmol/L NaCl + 0.1 mol/L  $H_2SO_4$ ), followed by the addition of poloxamer (red) ( $82 \mu\text{mol/L PEO}_2\text{PPO}_3\text{PEO}_2$  + 1 mmol/L NaCl + 0.1 mol/L  $H_2SO_4$ ). Disruption of the water modes by  $Cl^-$  adsorption (black) facilitates the subsequent co-adsorption of poloxamer (red) where water is displaced by the hydrophobic segments while the ethereal oxygen forms hydrogen bonds with the adjacent electrolyte.

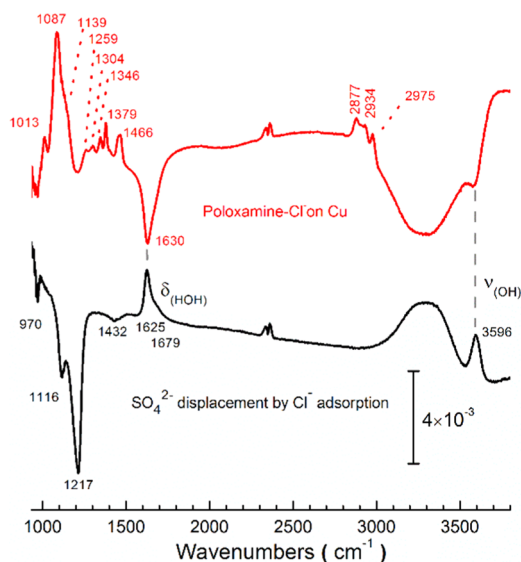


**Figure 11.** SEIRAS difference spectra at  $-0.65 V_{SSE}$  after  $Cl^-$  titration (black) (1 mmol/L NaCl + 0.1 mol/L  $H_2SO_4$ ) followed by the addition of poloxamine (red) ( $87 \mu\text{mol/L poloxamine}$  + 1 mmol/L NaCl + 0.1 mol/L  $H_2SO_4$ ). The disruption of the water modes by  $Cl^-$  adsorption (black) facilitates the subsequent co-adsorption of poloxamine (red) where water is displaced by the hydrophobic segments while the ethereal oxygen forms hydrogen bonds with the adjacent electrolyte.

poloxamine peak (Figure 11) also includes contributions from the aliphatic ethylenediamine core.

For reference purposes, spectra for the as-received neat liquid poloxamer (Figure S20a) and poloxamine (Figure S20b) were examined and found to be quite similar. Subtraction of the two spectra reveals contributions between 1020 and 1190  $\text{cm}^{-1}$  that are at least partly attributed to poloxamine C–N modes (Figure S20). For the suppressor layers, the peak energy of the multicomponent C–O–C peak envelope found at 1095

$\text{cm}^{-1}$  for adsorbed PEG– $Cl^-$  (Figure 9) shifts to 1088  $\text{cm}^{-1}$  for poloxamine– $Cl^-$  and 1084  $\text{cm}^{-1}$  for poloxamer– $Cl^-$ . The trend is opposite to that reported for solvated triblock PEO and PPO polymers, presumably due to the interaction with the halide adlayer.<sup>107</sup> The  $\text{CH}_2$  stretch modes between 2800 and 3000  $\text{cm}^{-1}$  are similar for the two polymers with the additional peak at 2976  $\text{cm}^{-1}$  for the antisymmetric stretch of the methyl groups in the PPO segments. Likewise, the symmetric  $\text{CH}_3$  umbrella mode of the PPO block is evident at 1379–1380  $\text{cm}^{-1}$ . Compared to more concentrated solution of larger poloxamers, the  $\text{CH}_3$  and  $\text{CH}_2$  band energies suggest that the adsorbed polymer has more in common with isolated chains than micelles.<sup>107</sup>

Curve fitting and area measurements of the C–O–C backbone and  $\text{CH}_2/\text{CH}_3$  stretch region of the respective polyether– $Cl^-$  suppressor layers as well as the neat references are summarized in Figures S21 and S22 and Tables S5 and S6. The ratio of the area of the large multicomponent C–O–C peak to that of the methylene stretch region for the adsorbed polyether– $Cl^-$  adlayer is 2.47 for the poloxamer and 3.67 for the poloxamine. The former is similar to the 2.5 for the PEG– $Cl^-$  adlayer (Table S4). In both cases, the ratio for the adsorbed layer is smaller than the 4.35 value of the neat, isotropic, liquid polymers. As with PEG, the decrease reflects the anisotropy introduced by adsorption of the respective polymers on the  $Cl^-$ -covered surface. The weaker change for the poloxamine is attributed to more limited molecular rearrangement during its adsorption due to constraints that arise from branching at the ethylenediamine core that give the polymer a more spherical motif. Compared to the respective neat forms, a relative decrease of the  $\sim 2866 \text{ cm}^{-1}$  and increase of the  $\sim 2932 \text{ cm}^{-1}$   $\text{CH}_2$  stretch modes is evident in Figures S21 and S22 for the block polyethers adsorbed on the  $Cl^-$ -covered surface. The anisotropy associated with polyether co-adsorption is also evident in the red shift of the C–O–C peak envelope of the respective polymers. Comparison to the solvated versions of the respective polyethers would be useful, but this awaits future investigation.

#### Poloxamer and Poloxamine Adsorption on Cu in the Absence of $Cl^-$ .

The importance of anion adsorption in the co-adsorption of poloxamer and poloxamine was examined by reversing the order of additive addition at  $-0.65 V_{SSE}$ . As shown in Figure 12a,b, the addition of  $82 \mu\text{mol/L}$  poloxamer to 0.1 mol/L  $H_2SO_4$  leads to weak adsorption similar to PEG, as evident by the small multicomponent peak near 1084  $\text{cm}^{-1}$ , the  $\text{CH}_3$  mode at 1379  $\text{cm}^{-1}$ , the scissor modes near 1450  $\text{cm}^{-1}$ , and the  $\text{CH}_2$  stretches between 2850 and 3000  $\text{cm}^{-1}$ . On the basis of the size of the latter two bands, the poloxamer coverage is  $\approx 34\%$  that observed for the poloxamer– $Cl^-$  surface. The small dip near 1217  $\text{cm}^{-1}$  in the poloxamer-only spectrum suggests that adsorption is accompanied by slight displacement of the  $\text{SO}_4^{2-}$  species. The potential dependence of  $\text{SO}_4^{2-}$  adsorption was thus examined and, as shown in Figure S23, a potential step to  $-0.55 V_{SSE}$  led to an increase in  $\text{SO}_4^{2-}$  coverage, followed by a decrease upon stepping to  $-0.8 V_{SSE}$ . The changes are almost identical to those observed for the polymer-free electrolyte. The slight difference in the  $\text{SO}_4^{2-}$  absorbance,  $\approx 2.5 \times 10^{-4}$  in Figure S23, is of the same order of magnitude as the decreased sulfate band,  $\approx 4 \times 10^{-4}$ , in the  $-0.65 V_{SSE}$  polymer titration spectrum in Figure 12a. Compared to the polymer-free spectrum in Figure S23, the small decrease near 1100 and 1450  $\text{cm}^{-1}$  at  $-0.8 V_{SSE}$  is due to a minor loss of the –C–C–O– backbone and  $\text{CH}_2$  scissor

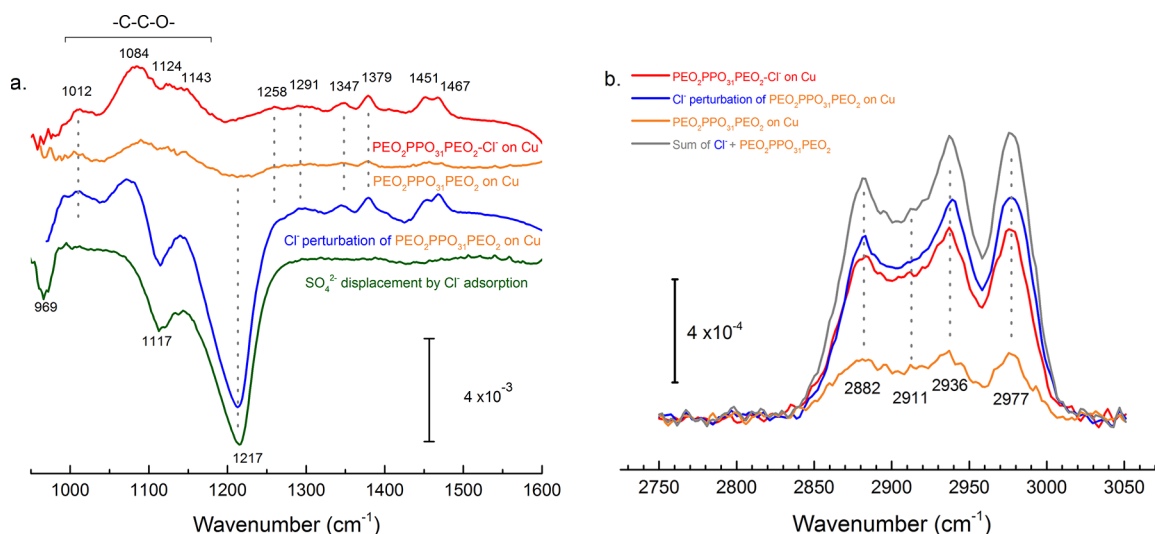


**Figure 12.** (a) PEO<sub>2</sub>PPO<sub>31</sub>PEO<sub>2</sub> backbone spectra based on the order of additive addition at  $-0.65 V_{SSE}$ ; PEO<sub>2</sub>PPO<sub>31</sub>PEO<sub>2</sub> addition to NaCl + H<sub>2</sub>SO<sub>4</sub> (red), PEO<sub>2</sub>PPO<sub>31</sub>PEO<sub>2</sub> addition to H<sub>2</sub>SO<sub>4</sub> (orange), NaCl addition to PEO<sub>2</sub>PPO<sub>31</sub>PEO<sub>2</sub> + H<sub>2</sub>SO<sub>4</sub> (blue), and NaCl to H<sub>2</sub>SO<sub>4</sub> (green). (b) Dependence of the methyl and methylene spectra on the order of additive titration at  $-0.65 V_{SSE}$ ; PEO<sub>2</sub>PPO<sub>31</sub>PEO<sub>2</sub> addition to NaCl + H<sub>2</sub>SO<sub>4</sub> (red), PEO<sub>2</sub>PPO<sub>31</sub>PEO<sub>2</sub> addition to H<sub>2</sub>SO<sub>4</sub> (orange), and NaCl addition to PEO<sub>2</sub>PPO<sub>31</sub>PEO<sub>2</sub> + H<sub>2</sub>SO<sub>4</sub> (blue). The final concentration of the respective additives in 0.1 mol/L H<sub>2</sub>SO<sub>4</sub> were 1 mmol/L NaCl and 82 μmol/L poloxamer.

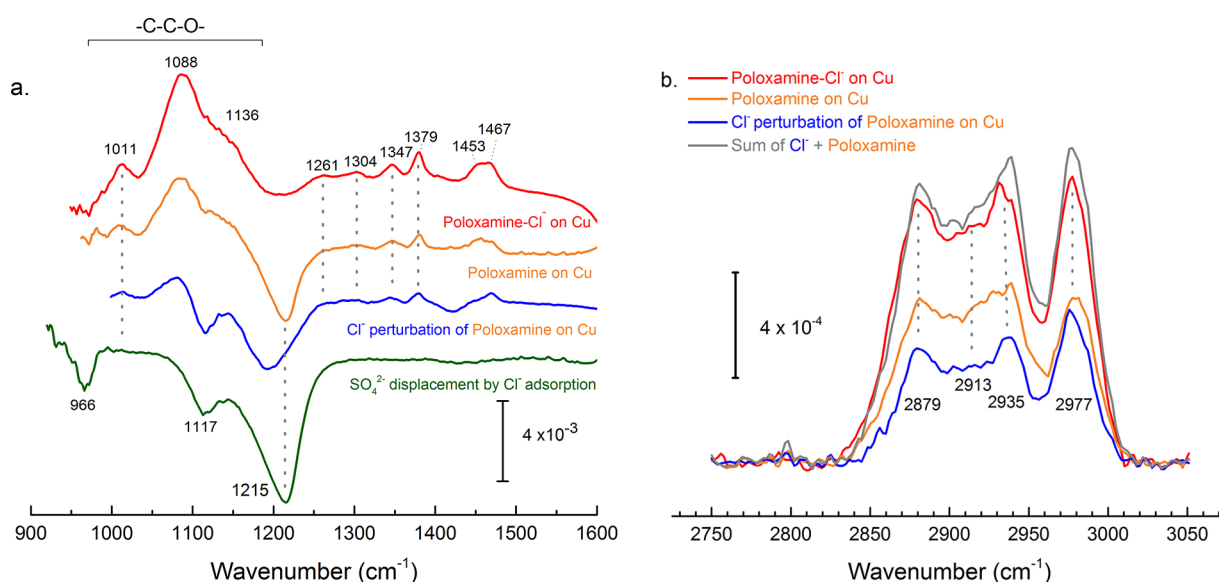


**Figure 13.** (a) Poloxamine backbone spectra based on the order of additive addition at  $-0.65 V_{SSE}$ ; poloxamine addition to NaCl + H<sub>2</sub>SO<sub>4</sub> (red), poloxamine addition to H<sub>2</sub>SO<sub>4</sub> (orange), NaCl addition to poloxamine + H<sub>2</sub>SO<sub>4</sub> (blue), and NaCl addition to H<sub>2</sub>SO<sub>4</sub> (green). (b) Dependence of the methyl and methylene spectra on the order of additive titration at  $-0.65 V_{SSE}$ ; poloxamine addition to NaCl + H<sub>2</sub>SO<sub>4</sub> (red), poloxamine addition to H<sub>2</sub>SO<sub>4</sub> (orange), and NaCl addition to poloxamine + H<sub>2</sub>SO<sub>4</sub> (blue). The final concentration of the respective additives in 0.1 mol/L H<sub>2</sub>SO<sub>4</sub> were 1 mmol/L NaCl and 87 μmol/L poloxamine.

modes upon rearrangement and desorption of a small amount of poloxamer.

In contrast to PEG and poloxamer, a larger increment of poloxamine adsorption occurs with its addition to 0.1 mol/L H<sub>2</sub>SO<sub>4</sub>, as shown in Figure 13a,b. The multicomponent polyether backbone mode at 1088 cm<sup>-1</sup> for C–O–C also includes C–N<sup>+</sup> contributions from the ethylenediamine core while the CH<sub>2</sub> wag at 1347 cm<sup>-1</sup>, CH<sub>3</sub> mode at 1379 cm<sup>-1</sup>, CH<sub>2</sub> scissor modes at 1453 and 1467 cm<sup>-1</sup>, and the CH stretch region between 2878 and 2976 cm<sup>-1</sup> are all resolved. The negative peak near 1225 cm<sup>-1</sup> marks the decrease in SO<sub>4</sub><sup>2-</sup> coverage that accompanies poloxamine adsorption. Examination of the SO<sub>4</sub><sup>2-</sup> potential dependence upon stepping from

$-0.65$  to  $-0.8$  or  $-0.55 V_{SSE}$  reveals a notably smaller change compared to the polymer-free system as shown in Figure S24. The adsorbed polymer results in a decrease in the SO<sub>4</sub><sup>2-</sup> coverage available for reversible adsorption/desorption. The interaction between SO<sub>4</sub><sup>2-</sup> and the protonated ethylenediamine C–N<sup>+</sup> core of the poloxamine is also evident in the change in the shape and position of the SO<sub>4</sub><sup>2-</sup> band. However, no other changes in the polymer modes were resolved for the potential range examined.

**Influence of Cl<sup>-</sup> Additions on Poloxamer and Poloxamine Adsorption.** As with PEG, the addition of Cl<sup>-</sup> to the poloxamer solutions results in significant changes in the difference spectra, as shown in Figure 12 (and Figure S25).

Complete displacement of the  $\text{SO}_4^{2-}$  species by  $\text{Cl}^-$  adsorption occurs as indicated by the negative peaks centered at 1217, 1117, and  $969\text{ cm}^{-1}$  similar to the spectra for  $\text{SO}_4^{2-}$  displacement by  $\text{Cl}^-$  in the polymer-free electrolyte. Halide adsorption is accompanied by an increased intensity for the 1012 and  $1084\text{ cm}^{-1}$  bands associated with the  $-\text{C}-\text{C}-\text{O}-$  backbone modes although the latter is somewhat obscured by overlap with the  $\text{SO}_4^{2-}$  desorption peak. Likewise, an increase in the  $\text{CH}_2$  twist at  $1291\text{ cm}^{-1}$ , the  $\text{CH}_2$  wag near  $1347\text{ cm}^{-1}$ , the  $\text{CH}_3$  mode at  $1379\text{ cm}^{-1}$ , and the scissor bands at 1451 and  $1467\text{ cm}^{-1}$  are evident along with the substantial increase in the  $\text{CH}_2$  stretch modes between 2850 and  $3000\text{ cm}^{-1}$ . The  $\text{Cl}^-$ -stimulated desorption of  $\text{SO}_4^{2-}$  and co-adsorption of the poloxamer are accompanied by displacement of hydronium and the water modes, both hydrogen-bonded and non-hydrogen-bonded, as shown in Figure S25.

Similar trends are evident with the addition of  $\text{Cl}^-$  to the poloxamine-containing electrolyte, as shown in Figure 13. Compared to PEG and poloxamer, the increment of polymer adsorption is smaller due to the higher initial polymer coverage. Nonetheless, with the  $\text{Cl}^-$  addition, the remaining  $\text{SO}_4^{2-}$  is displaced and the poloxamine multicomponent polyether backbone band increases along with the  $\text{CH}_2$  wag near  $1347\text{ cm}^{-1}$ ,  $\text{CH}_3$  mode at  $1379\text{ cm}^{-1}$ , and the scissor bands at 1453 and  $1467\text{ cm}^{-1}$ . As with the lower-wavenumber spectra, the intensities of the  $\text{CH}_2$  and  $\text{CH}_3$  stretch band increase with the addition of  $\text{Cl}^-$ , almost doubling the poloxamine coverage consistent with the related loss of  $\text{SO}_4^{2-}$  bands with sequential poloxamine and  $\text{Cl}^-$  addition. Linear combination of the poloxamine spectra with that following  $\text{Cl}^-$  addition matches the intensity associated with the inverse order of additions. Thus, the final poloxamine- $\text{Cl}^-$  layer is not dependent on the history of additive addition. As with the other polyethers, displacement  $\text{SO}_4^{2-}-\text{H}_3\text{O}^+/\text{H}_2\text{O}$  by halide addition is accompanied by significant loss in the hydronium and water modes coincident with the formation of the saturated poloxamine- $\text{Cl}^-$  layer, as shown in Figure S26.

**Discussion.** Water-soluble polymers play a major role in many aspects of surface science and surfactant technology. Solvation of polyethers is intimately associated with hydrogen bond formation with ethereal oxygen, while their surfactant activity is related to interfacial water structure that is responsive to different surfaces and related chemistry.<sup>50,51</sup> For Cu electrodeposition, the present experiments indicate an important role of anion-mediated changes in interface hydrophobicity in polyether co-adsorption. This insight stands in contrast to prior efforts that focused on  $\text{Cu}^+$ -ether-mediated binding to Cu surfaces.<sup>10,36,37</sup>

SEIRAS measurements reveal the profound effect of anion adsorption on the water structure at Cu surfaces. At  $-0.65\text{ V}_{\text{SSE}}$  in 0.1 mol/L  $\text{H}_2\text{SO}_4$ , a mixed  $\text{SO}_4^{2-}-\text{H}_3\text{O}^+/\text{H}_2\text{O}$  adlayer forms on Cu(111) that when ordered is isosymmetric with that reported for other fcc (111) surfaces.<sup>57,58,64-68</sup> For the Cu thin films studied herein, the potential-dependent coverage of the sulfate adlayer is similar to that reported for Cu(111).<sup>57,58</sup> The differences that remain are presumably associated with finite terrace size and dispersion of orientations associated with the PVD films. When halide is added to the electrolyte, the co-adsorbed  $\text{SO}_4^{2-}-\text{H}_3\text{O}^+/\text{H}_2\text{O}$  is displaced as  $\text{Cl}^-$  rapidly forms a compact ordered adlayer on the low-index surface segments. Previous STM studies reveal that this is accompanied by significant step faceting and coarsening with time.<sup>21-27</sup> The ordered halide adlayer on the Cu thin film gives rise to a

narrow vibrational band near  $3600\text{ cm}^{-1}$  congruent with significant non-hydrogen-bonded water with the net positive dipole of O-H being oriented toward the  $\text{Cl}^-$ -covered Cu surface. The  $-100\text{ cm}^{-1}$  red shift to  $3600\text{ cm}^{-1}$  compared to that of free  $\text{OH}^-$  species observed at the water-air interface ( $3700\text{ cm}^{-1}$ ) may be associated with the halide charge.<sup>52,54,55,80,81,87</sup> In addition to free OH, "labile"  $\text{H}_2\text{O}$  (with neither H involved in hydrogen bonding) with its net molecular dipole oriented close to the surface normal has also been reported near  $3600\text{ cm}^{-1}$ .<sup>54,73</sup> In either case, the halide adlayer clearly serves to stabilize non-hydrogen water at the interface. Following halide titration, the non-hydrogen-bonded water mode rises rapidly, followed by a much slower evolution of the hydrogen-bonded water over a time scale of minutes. The latter maybe related to further templating of the water structure as the domain size of the ordered halide layer increases with slow coarsening of the mesoscale surface features. Similar reports of the sensitivity of water modes to reorganization of surface structure exist for Au surfaces.<sup>72,84</sup> Most importantly, several vibrational spectroscopy studies of water-air and water-solvent interfaces suggest an association between the development of non-hydrogen-bonded, dangling "free" OH and hydrophobic behavior.<sup>52,54,55,80-82</sup> It follows that the high surface tension of water is intimately related to disruption of its hydrogen bond network. The amphiphilic nature of PEG is such that the disrupted water structure associated with the halide-covered Cu surface can be effectively dissipated by polyether segregation to the interface, whereby the hydrophobic  $\text{CH}_2-\text{CH}_2$  components are biased toward the halide layer, while the ethereal oxygen sites are available for hydrogen bonding with the adjacent water network.

PEG co-adsorption on the  $\text{Cl}^-$ -covered Cu surface, as reflected in the  $-\text{C}-\text{C}-\text{O}-$  backbone,  $\text{CH}_2$  twist, and  $\text{CH}_2$  wag modes, results in significant deviations from the water-stabilized T-G-T,  $-\text{O}-\text{C}-\text{C}-\text{O}-$  helical conformation associated with its solubility in water. Specifically, the increase in G (gauche) arrangement around the ethereal C-O-C bond, indicated by the backbone mode at  $1030\text{ cm}^{-1}$  and the  $\text{CH}_2$  twist at  $1307\text{ cm}^{-1}$ , reflects the disruption of the helical backbone. Even in the absence of water, studies of energy funneling during melting of helical PEG point to C-O bond rotation as the more favored deformation path.<sup>108</sup> In the present case, the hydrophobic nature of the  $\text{Cl}^-$ -terminated surface induces restructuring of the polymer's secondary structure during adsorption. Specifically, the alkyl and ethereal groups of the adsorbed molecule are biased toward the inner and outer sides of the double layer to mediate the hydrophobic and hydrophilic interactions between the  $\text{Cl}^-$ -covered metal and the electrolyte, respectively. Looking beyond PEG, the nonpolar PPO segments of the poloxamer and poloxamine provide further driving force for segregation and stabilization of the respective polymers to hydrophobic surfaces, thereby enhancing the polyether suppression of the Cu deposition reaction on halide-covered surfaces.

The above suggests an alternative approach to enhancing the suppressor action, namely, pretreating bare Cu surfaces with a hydrophobic methyl-terminated short alkyl chain thiol prior to electroplating in the presence of PEG. When this is done, significantly greater inhibition is observed due to the co-adsorption of PEG that blocks residual pin holes in the underlying hydrophobic monolayer systems.<sup>109</sup> As detailed in the supplement (Figure S27), these hydrophobic methylated surfaces support PEG adsorption, although the conformation

of the co-adsorbed polyether and resulting metal deposition processes are distinctly different from those associated with the halide-covered surface. More broadly, the impact of substrate hydrophilicity on the adsorption of PEG, PPG, and a triblock poloxamer on prototypical surfaces, such as hydrophilic silica and hydrophobic polystyrene, has been examined in detail.<sup>50,51</sup> Specifically, SFG measurements of the CH<sub>3</sub> and CH<sub>2</sub> stretch region indicate no quantifiable change in the secondary structure of polyethers during weak adsorption on silica, while significant anisotropy accompanies polyether assembly on hydrophobic polystyrene.<sup>50</sup> The measurements were congruent with the adsorbed polyethers having their hydrophobic components oriented toward the hydrophobic substrate surface. Further examination of polyether adsorption from methanol solutions indicated that the interaction of water with the hydrophobic surfaces was a key element in the anisotropic adsorption of the polyether. In a related fashion, a correlation between halide adsorption and hydrophobic character was previously inferred from the rapid assembly of ordered porphyrins and related 2D molecules on halide-covered Au(111) surfaces.<sup>110</sup> The resulting adsorbate structures are analogous to those reported on other hydrophobic van der Waals solids.

The potential dependence of halide adsorption on Cu provides an excellent avenue for exploring polyether co-adsorption.<sup>21,25,29</sup> At negative potentials, the Cl<sup>-</sup> adlayer formed on low-index Cu surfaces undergo order–disorder phase transitions with significant halide desorption. SEIRAS measurements reveal that this is accompanied by disruption of the neighboring non-hydrogen-bonding water. In the presence of polyethers, stepping to negative potentials results in some disruption of the polymer layer and corresponding alteration of the water modes. In the presence of both additives, the halide layer is somewhat stabilized by the polymer as the order–disorder phase transition is shifted, –50 mV, to more negative potentials, as revealed by voltammetric and SXS studies.<sup>19,29</sup> From an application perspective, the link between the halide order–disorder phase transition, water structure, and polyether adsorption underlies the critical phenomena associated with breakdown of the polyether–Cl<sup>-</sup> suppressor layer that is central to bottom-up filling of Cu TSV.<sup>5,17,18,25</sup> Presently, there are numerous efforts underway to develop physically robust models of the associated dynamics.<sup>5–7,17,18,25</sup> What if any role cations, such as Cu<sup>2+</sup> or, more importantly, its hydrated form, play in suppressor film formation and operation remains to be resolved. Recent studies of specific ion effects on polymer aggregation, i.e., Hofmeister series, indicate that divalent, but not monovalent ions, affect the micellization and aggregation of poloxamers at higher temperatures.<sup>111</sup> Future work examining supporting electrolyte effects may be helpful in addressing this question.

Further insight into the nature of polyether adsorption has also been obtained by examining its displacement by competitive adsorption of hydrophilic sulfonate-terminated short alkyl chain disulfide (SPS) or thiol (MPS) molecules.<sup>3,4,15,19</sup> SEIRAS experiments that explore the functional role of the accelerator will be detailed in a companion paper. Briefly, competitive adsorption of hydrophilic accelerator species results in a progressive disruption of the initially formed PEG–Cl<sup>-</sup> layer and the Cu deposition kinetics evolves toward that of an unsuppressed system.<sup>3,4,15,19</sup> Accordingly, it is the competitive interaction between hydrophobic PEG–Cl<sup>-</sup> and hydrophilic SPS/MPS species that provides the chemical

basis of the curvature-enhanced accelerator mechanism that underlies superconformal electrodeposition of Cu.

## CONCLUSIONS

Superconformal electrodeposition is a key process in the fabrication of microelectronics interconnects from the nano-scale devices to printed circuit boards. The process depends on additives that suppress and accelerate the local growth rate while producing Cu deposits free of undue contamination. Co-adsorption of polyethers and Cl<sup>-</sup> on Cu provides suppression of the metal deposition process by hindering access of Cu<sup>2+</sup> to the metal surface. The combination of potential difference and titration SEIRAS measurements provide new insights into the polyether–halide co-adsorption process. In 0.1 mol/L H<sub>2</sub>SO<sub>4</sub>, a potential-dependent mixed SO<sub>4</sub><sup>2-</sup>–H<sub>3</sub>O<sup>+</sup>/H<sub>2</sub>O layer forms on weakly textured (111) Cu thin-film surfaces. Limited polyether adsorption occurs on the hydrophilic oxyanion layer congruent with the absence of significant inhibition of metal deposition under such conditions. However, with the addition of Cl<sup>-</sup>, the SO<sub>4</sub><sup>2-</sup>–H<sub>3</sub>O<sup>+</sup>/H<sub>2</sub>O adlayer is displaced and an ordered halide layer rapidly forms. The halide layer exerts a profound effect on the adjacent solvent network, with the adsorbed halide giving rise to an increase in non-hydrogen-bonded water that makes the interface more hydrophobic. In the presence of the polyether, the altered wetting behavior induced by halide adsorption tips the balance in favor of polyether co-adsorption. Water is displaced from the interface as the hydrophobic portions of the polyether molecule assemble on the Cl<sup>-</sup>-covered surface while the lone pair electrons of the ethereal oxygen are available for forming hydrogen bonds with the solvent network in the electrolyte. The same trends are evident for polyethers with different tertiary structures, from linear PEG to the triblock copolymer polyoxamer PEO<sub>2</sub>PPO<sub>31</sub>PEO<sub>2</sub> to the branched, block copolymer polyoxamine (PEO<sub>4</sub>PPO<sub>12</sub>)<sub>2</sub>N(CH<sub>2</sub>)<sub>2</sub>N(PPO<sub>12</sub>PEO<sub>4</sub>)<sub>2</sub>.

## ASSOCIATED CONTENT

### Supporting Information

The Supporting Information is available free of charge on the ACS Publications website at DOI: 10.1021/acs.jpcc.8b06644.

Single beam spectra; scanning electron micrograph; SEIRAS spectra; Stark tuning shifts; ATR difference spectra; absorbance vs SO<sub>4</sub><sup>2-</sup> concentration; SEIRAS difference spectra; intensity of a selected bands for solvated PEG; reference spectra; fingerprint region; peak deconvolution; potential difference spectra; SEIRAS titration spectra; (Figures S1–S27); spectral references for sulfate and bisulfate, solvated PEG and dPEG, PEG and dPEG powder; peak fit parameters (Tables S1–S6); PEG adsorption on propanethiol terminated Cu (PDF)

## AUTHOR INFORMATION

### Corresponding Author

\*E-mail: thomas.moffat@nist.gov.

### ORCID

Shouzhong Zou: 0000-0003-1952-8799

Lee J. Richter: 0000-0002-9433-3724

Thomas P. Moffat: 0000-0003-4377-1692

### Present Addresses

‡American University, Washington, DC 20016, United states (S.Z.).

<sup>†</sup>State Key Laboratory of Marine Environmental Science, College of the Environment and Ecology, Xiamen University, Xiamen 361002, China (G.-K.L.).

## Notes

The authors declare no competing financial interest.

## ■ ADDITIONAL NOTE

<sup>a</sup>Identification of commercial products in this paper is done to specify the experimental procedure. In no case does this imply endorsement or recommendation by the National Institute of Standards and Technology.

## ■ REFERENCES

- (1) Andricacos, P. C.; Uzoh, C.; Dukovic, J. O.; Horkans, J.; Deligianni, H. Damascene Copper Electroplating for Chip Interconnections. *IBM J. Res. Dev.* **1998**, *42*, 567–574.
- (2) Gambino, J. P.; Adderly, S. A.; Knickerbocker, J. U. An Overview of Through-Silicon-Via Technology and Manufacturing Challenges. *Microelectron. Eng.* **2015**, *135*, 73–106.
- (3) Moffat, T. P.; Wheeler, D.; Edelstein, M. D.; Josell, D. Superconformal Film Growth: Mechanism and Quantification. *IBM J. Res. Dev.* **2005**, *49*, 19–36.
- (4) Moffat, T. P.; Wheeler, D.; Josell, D. Superfilling and the Curvature Enhanced Accelerator Coverage Mechanism. *Interface* **2004**, *13* (4), 46–52.
- (5) Moffat, T. P.; Josell, D. Extreme Bottom-Up Superfilling of Through-Silicon-Vias by Damascene Processing: Suppressor Disruption, Positive Feedback and Turing Patterns. *J. Electrochem. Soc.* **2012**, *159*, D208–D216.
- (6) Josell, D.; Wheeler, D.; Moffat, T. P. Modeling Extreme Bottom-Up Filling of Through Silicon Vias. *J. Electrochem. Soc.* **2012**, *159*, D570–D576.
- (7) Wheeler, D.; Moffat, T. P.; Josell, D. Spatial-Temporal Modeling of Extreme Bottom-up Filling of Through-Silicon-Vias. *J. Electrochem. Soc.* **2013**, *160*, D3260–D3265.
- (8) Yang, L.; Radisic, A.; Deconinck, J.; Vereecken, P. M. Modeling the Bottom-Up Filling of Through Silicon Vias Through Suppressor Adsorption/Desorption Mechanism. *J. Electrochem. Soc.* **2013**, *160*, D3051–D3056.
- (9) Hill, M. R. H.; Rogers, G. T. Polyethylene Glycol in Copper Electrodeposition Onto a Rotating Disk Electrode. *J. Electroanal. Chem. Interfacial Electrochem.* **1978**, *86*, 179–188.
- (10) Yokoi, M.; Konishi, S.; Hayashi, T. Adsorption Behavior of Polyoxyethylene-glycol on the Copper Surface in Acid Copper-Sulfate Bath. *Denki Kagaku* **1984**, *52*, 218–223.
- (11) Kelly, J. J.; West, A. C. Copper Deposition in the Presence of Polyethylene Glycol. I. Quartz Crystal Microbalance Study. *J. Electrochem. Soc.* **1998**, *145*, 3472–3476.
- (12) Hebert, K. R. Role of Chloride in Suppression of Copper Electrodeposition by Polyethylene Glycol. *J. Electrochem. Soc.* **2005**, *152*, C283–C287.
- (13) Willey, M. J.; West, A. C. Microfluidic Studies of Adsorption and Desorption of Polyethylene Glycol During Copper Electrodeposition. *J. Electrochem. Soc.* **2006**, *153*, C728–C734.
- (14) Garrido, M. E. H.; Pritzker, M. D. Inhibition of Copper Deposition by Polyethylene Glycol and Chloride. I. Model Development and Parameter Estimation. *J. Electrochem. Soc.* **2009**, *156*, D36–D44.
- (15) Gallaway, J. W.; Willey, M. J.; West, A. C. Acceleration Kinetics of PEG, PPG and a Triblock Copolymer by SPS During Copper Electroplating. *J. Electrochem. Soc.* **2009**, *156*, D146–D154.
- (16) Garrido, M. E. H.; Pritzker, M. D. Inhibition of Copper Deposition by Polyethylene Glycol and Chloride. II. Analysis and Application. *J. Electrochem. Soc.* **2009**, *156*, D175–D183.
- (17) Yang, L.; Radisic, A.; Deconinck, J.; Vereecken, P. M. Stochastic Modeling of Polyethylene Glycol as a Suppressor in Copper Electroplating. *J. Electrochem. Soc.* **2014**, *161*, D269–D276.
- (18) Yang, H.; Dianat, A.; Bobeth, M.; Cuniberti, G. Copper Electroplating with Polyethylene Glycol. I. An Alternative Hysteresis Model without Additive Consumption. *J. Electrochem. Soc.* **2017**, *164*, D196–D203.
- (19) Moffat, T. P.; Yang, L.-Y. O. Accelerator Surface Phase Associated with Superconformal Cu Electrodeposition. *J. Electrochem. Soc.* **2010**, *157*, D228–D241.
- (20) Huynh, T. M. T.; Hai, N. T. M.; Broekmann, P. Quasi-Reversible Interaction of MPS and Chloride on Cu (100) Studied by In Situ STM. *J. Electrochem. Soc.* **2013**, *160*, D3063–D3069.
- (21) Magnussen, O. M. Ordered Anion Adlayers on Metal Electrode Surfaces. *Chem. Rev.* **2002**, *102*, 679–725.
- (22) Vogt, M. R.; Moller, F. A.; Schilz, C. M.; Magnussen, O. M.; Behm, R. J. Adsorbate-induced Step Faceting of Cu (100) Electrodes in HCl. *Surf. Sci.* **1996**, *367*, L33–L41.
- (23) Moffat, T. P. In *Nanostructured Materials in Electrochemistry*, Electrochemical Society Proceedings, 1995; Vol. 95–98, 225–236.
- (24) Moffat, T. P. An STM Study of the Influence of Step-Common:author-query>AQ8: Please provide a DOI number for ref 24 or indicate if one doesn't exist.</tep-common:author-query>of Adsorption on Step Dynamics. *Mater. Res. Soc. Symp. Proc.* **1997**, *451*, 75–80.
- (25) Moffat, T. P. In *STM Studies of Halide Adsorption on Cu (100), Cu (110) and Cu (111)*, Electrochemical Processing in ULSI Fabrication and Semiconductor/metal Deposition II. The Electrochemical Society Proceedings, 1999; Vol 99-9, pp 41–51.
- (26) Broeckmann, P.; Wilms, M.; Arenz, M.; Spänig, A.; Wandelt, K. Atomic Structure of Cu(111) Surfaces in Dilute Sulfuric Acid Solution. In *Solid–Liquid Interfaces, Macroscopic Phenomena — Microscopic Understanding*; Wandelt, K., Thurgate, S., Eds.; Topics in Applied Physics; Springer: New York, 2003; Vol. 85, pp 141–197.
- (27) Stuhlmann, C.; Wohlmann, B.; Park, Z.; Kruft, M.; Broekmann, P.; Wandelt, K. Chloride Adsorption on Cu(111) Electrodes: Electrochemical Behavior and UHV Transfer Experiments. In *Solid–Liquid Interfaces, Macroscopic Phenomena — Microscopic Understanding*; Wandelt, K., Thurgate, S., Eds.; Topics in Applied Physics; Springer: New York, 2003; Vol. 85, pp 199–221.
- (28) Keller, H.; Saracino, M.; Nguyen, H. M. T.; Huynh, T. M. T.; Broekmann, P. Competitive Anion/Water and Cation/Water Interaction at Electrified Copper/Electrolyte Interfaces Probed by In Situ X-ray Diffraction. *J. Phys. Chem. C* **2012**, *116*, 11068–11976.
- (29) Golks, F.; Grunder, Y.; Drunkler, A.; Roy, J.; Stettner, J.; Zegenhagen, J.; Magnussen, O. M. In Situ Surface X-Ray Diffraction Studies of the Influence of the PEG-Cl-Complex on Homoepitaxial Electrodeposition of Cu (001). *J. Electrochem. Soc.* **2013**, *160*, D3165–D3170.
- (30) Gründer, Y.; Kaminski, D.; Golks, F.; Krug, K.; Stettner, J.; Magnussen, O. M.; Franke, A.; Stremme, J.; Pehlke, E. Reversal of Chloride-induced Cu (001) Subsurface Buckling in the Electrochemical Environment, An In Situ Surface x-ray Diffraction and Density Functional Theory Study. *Phys. Rev. B* **2010**, *81*, No. 174114.
- (31) Gründer, Y.; Drunkler, A.; Golks, F.; Wijts, G.; Stettner, J.; Zegenhagen, J.; Magnussen, O. M. Cu (111) in Chloride Containing Acidic Electrolytes: Coadsorption of an Oxygenated Species. *J. Electroanal. Chem.* **2014**, *712*, 74–81.
- (32) Nagy, Z.; Blaudeau, J. P.; Hung, N. C.; Curtiss, L. C.; Zurawski, D. J. Chloride Ion Catalysis of the Copper Deposition Reaction. *J. Electrochem. Soc.* **1995**, *142*, L87–L89.
- (33) Yokoi, M.; Konishi, S.; Hayashi, T. Mechanism of the Electrodeposition and Dissolution of Copper in an Acid Copper-Sulfate Bath. 5. Acceleration Mechanism in the Presence of Cl<sup>-</sup> Ions. *Denki Kagaku* **1983**, *51*, 460–464.
- (34) Walker, M. L.; Richter, L. J.; Moffat, T. P. In situ Ellipsometric Study of PEG/Cl<sup>-</sup> Coadsorption on Cu, Ag and Au. *J. Electrochem. Soc.* **2005**, *152*, C403–C407.
- (35) Doblhofer, K.; Wasle, S.; Soares, D. M.; Weil, K. G.; Weinberg, G.; Ertl, G. The Influence of Halide Ions on the Kinetics of Electrochemical Copper (II) Reduction. *Z. Phys. Chem.* **2003**, *217*, 479–449.

- (36) Feng, Z. V.; Li, X.; Gewirth, A. A. Inhibition Due to the Interaction of Polyethylene Glycol, Chloride and Copper in Plating baths: A Surface-Enhanced Raman Study. *J. Phys. Chem. B* **2003**, *107*, 9415–9423.
- (37) Hebert, K. R.; Adhikari, S.; Houser, J. E. Chemical Mechanism of Suppression of Copper Electrodeposition by Poly(ethylene glycol). *J. Electrochem. Soc.* **2005**, *152*, C324–C329.
- (38) Dow, W.-P.; Yen, M.-Y.; Lin, W.-B.; Ho, S.-W. Influence of Molecular Weight of Polyethylene Glycol on Microvia Filling by Copper Electroplating. *J. Electrochem. Soc.* **2005**, *152*, C769–C775.
- (39) Healy, J. P.; Pletcher, D.; Goodenough, M. The Chemistry of the Additives in an Acid Copper Electroplating Bath, Part I. Polyethylene Glycol and Chloride Ion. *J. Electroanal. Chem.* **1992**, *338*, 155–165.
- (40) Hope, G. A.; Brown, G. M. In *A Study of the Adsorption of Polymeric Additive at a Copper Electrode and Their Incorporation into Copper Deposits by Electrodeposition*, Proceedings of the 6th International Symposium on Electrode Processes, The Electrochemical Society Series, 1996; pp 215–226.
- (41) Petri, M.; Kolb, D. M.; Memmert, U.; Meyer, H. Adsorption of PEG on Au (111) Single-Crystal Electrodes and Its Influence on Copper Deposition. *J. Electrochem. Soc.* **2004**, *151*, C793–C797.
- (42) Fu, Y.; Pao, T.; Chen, S.-Z.; Yau, S.; Dow, W.-P.; Lee, Y.-L. Electrodeposition of Copper on a Pt (111) Electrode in Sulfuric Acid Containing Poly(ethylene glycol) and Chloride Ions as Probed by in Situ STM. *Langmuir* **2012**, *28*, 10120–10127.
- (43) Li, L.-H.; Yau, S.; Dow, W.-P. In situ STM Imaging of Polyethylene Glycol Adsorbed on an Au (111) Electrode in pH 3. *Electrochem. Commun.* **2016**, *70*, 1–4.
- (44) Skaug, M. J.; Mabry, J. N.; Schwartz, D. K. Single-Molecule Tracking of Polymer Surface Diffusion. *J. Am. Chem. Soc.* **2014**, *136*, 1327–1332 and references therein.
- (45) Scheutjens, J. M. H. M.; Fleer, G. J. Statistical Theory of the Adsorption of Interacting Chain Molecules. 2. Train, Loop and Tail Size Distribution. *J. Phys. Chem.* **1980**, *84*, 178–190.
- (46) Kim, Y.; Chae, M.-K.; Lee, N.-K.; Jung, Y.; Johner, A. Irreversible Adsorption of Wormlike Chains: Alignment Effects. *Macromolecules* **2017**, *50*, 6285–6292.
- (47) Chai, L.; Goldberg, R.; Kampf, N.; Klein, J. Selective Adsorption of Poly(ethylene oxide) Onto a Charged Surface Mediated by Alkali Metal Ions. *Langmuir* **2008**, *24*, 1570–1576.
- (48) Pattanayek, S. K.; Juvekar, V. A. Prediction of Adsorption of Nonionic Polymers from Aqueous Solutions to Solid Surfaces. *Macromolecules* **2002**, *35*, 9574–9585.
- (49) Tasaki, K. Poly(oxyethylene)-cation Interactions in Aqueous Solution: A Molecular Dynamics Study. *Comput. Theor. Polym. Sci.* **1999**, *9*, 271–284.
- (50) Kim, J.; Opdahl, A.; Chou, K. C.; Somorjai, G. A. Hydrophobic-Interaction-Induced Alignment of Polymers at the Solid/Liquid Interface Studied by Infrared-Visible Sum Frequency Generation. *Langmuir* **2003**, *19*, 9551–9553.
- (51) Chen, C.-Y.; Even, M. A.; Wang, J.; Chen, Z. Sum Frequency Generation Vibrational Spectroscopy Studies on Molecular Conformation of Liquid Polymers Poly(ethylene glycol) and Poly(propylene glycol) at Different Interfaces. *Macromolecules* **2002**, *35*, 9130–9135.
- (52) Björneholm, O.; Hansen, M. H.; Hodgson, A.; Liu, L.-M.; Limmer, D. T.; Michaelides, A.; Pedevilla, P.; Rossmel, J.; Shen, H.; Tocci, G.; et al. Water at Interfaces. *Chem. Rev.* **2016**, *116*, 7698–7726 and references therein.
- (53) Osawa, M. In situ Surface-Enhanced Infrared Spectroscopy of the Electrode/Solution Interface. In *Diffraction and Spectroscopic Methods in Electrochemistry*; Alkire, R. C., Kolb, D. M., Lipkowski, J., Ross, P. N., Eds.; Advances in Electrochemical Science and Engineering; Wiley-VCH, 2006; Chapter 8, Vol. 9, pp 269–314.
- (54) Scatena, L. F.; Brown, M. G.; Richmond, G. L. Water at Hydrophobic Surfaces: Weak Hydrogen Bonding and Strong Orientation Effects. *Science* **2011**, *292*, 908–911.
- (55) Du, Q.; Freysz, E.; Shen, Y. R. Surface Vibrational Spectroscopic Studies of Hydrogen Bonding and Hydrophobicity. *Science* **1994**, *264*, 826–828.
- (56) Enders, D.; Nagao, T.; Pucci, A.; Nakayama, T.; Aono, M. Surface-enhanced ATR-IR Spectroscopy with Interface Grown Plasmonic Gold Island Films Near the Percolation Threshold. *Phys. Chem. Chem. Phys.* **2011**, *13*, 4935–4941.
- (57) Lennartz, M.; Broekmann, P.; Arenz, M.; Stuhlmann, C.; Wandelt, K. Sulfate Adsorption of Cu (111) Studied by In-Situ IRRAS and STM: Revealing the Adsorption Site and Desorption Behavior. *Surf. Sci.* **1999**, *442*, 215–222.
- (58) Arenz, M.; Broekmann, P.; Lennartz, M.; Vogler, E.; Wandelt, K. In-situ Characterization of Metal/Electrolyte Interfaces: Sulfate Adsorption on Cu (111). *Phys. Status Solidi A* **2001**, *187*, 63–74.
- (59) Łukomska, A.; Sobkowski, J. Potential of Zero Charge of Monocrystalline Copper Electrodes in Perchlorate Solutions. *J. Electroanal. Chem.* **2004**, *567*, 95–102.
- (60) Brown, G. M.; Hope, G. A. A SERS Study of  $\text{SO}_4^{2-}/\text{Cl}^-$  Ion Adsorption at a Copper Electrode In-Situ. *J. Electroanal. Chem.* **1996**, *405*, 211–216.
- (61) Lachenwitzer, A.; Li, N.; Lipkowski, J. Determination of the Acid Dissociation Constant for Bisulfate Adsorbed at the Pt (111) Electrode by Subtractively Normalized Interfacial Fourier Transform Infrared Spectroscopy. *J. Electroanal. Chem.* **2002**, *532*, 85–98.
- (62) Niaura, G.; Malinauskas, A. Surface-enhanced Raman Spectroscopy of  $\text{ClO}_4^-$  and  $\text{SO}_4^{2-}$  Anions Adsorbed at a Cu Electrode. *J. Chem. Soc., Faraday Trans.* **1998**, *94*, 2205–2211.
- (63) Hope, G. A.; Woods, R. Transient Adsorption of Sulfate Ions During Copper Electrodeposition. *J. Electrochem. Soc.* **2004**, *151*, C550–C553.
- (64) Ito, M. Structures of Water at Electrified Interfaces: Microscopic Understanding of Electrode Potential in Electric Double Layers on Electrode Surfaces. *Surf. Sci. Rep.* **2008**, *63*, 329–389.
- (65) Shingaya, Y.; Ito, M. Comparison of a Bisulfate Anion Adsorbed on M (111) (M = Pt, Rh, Au, Ag and Cu). *J. Electroanal. Chem.* **1999**, *467*, 299–306.
- (66) Nakamura, M.; Kato, H.; Hoshi, N. Infrared Spectroscopy of Water Adsorbed on M (111) (M = Pt, Pd, Rh, Au, Cu) Electrodes in Sulfuric Acid Solution. *J. Phys. Chem. C* **2008**, *112*, 9458–9463.
- (67) Jinnouchi, R.; Hatanaka, T.; Morimoto, Y.; Osawa, M. First Principles Study of Sulfuric Acid Anion Adsorption on a Pt (111) Electrode. *Phys. Chem. Chem. Phys.* **2012**, *14*, 3208–3218.
- (68) Jinnouchi, R.; Hatanaka, T.; Morimoto, Y.; Osawa, M. Stark Effect on Vibrational Frequencies of Sulfate on Pt (111) Electrode. *Electrochim. Acta* **2013**, *101*, 254–261.
- (69) Comas-Vives, A.; Bandler, J.; Jacob, T. Ab Initio Study of the Electrochemical  $\text{H}_2\text{SO}_4/\text{Pt}$  (111) Interface. *Phys. Chem. Chem. Phys.* **2013**, *15*, 992–997.
- (70) Ataka, K.; Yotsuyanagi, T.; Osawa, M. Potential-Dependent Reorientation of Water Molecules at an Electrode/Electrolyte Interface Studied by Surface-Enhanced Infrared Absorption Spectroscopy. *J. Phys. Chem.* **1996**, *100*, 10664–10672.
- (71) Ataka, K.; Osawa, M. In Situ Infrared Study of Water-Sulfate Co-adsorption on Au (111) in Sulfuric Acid Solutions. *Langmuir* **1998**, *14*, 951–959.
- (72) Garcia-Araez, N.; Rodriguez, P.; Navarro, V.; Bakker, H. J.; Koper, M. T. Structural Effects on Water Adsorption on Gold Electrodes. *J. Phys. Chem. C* **2011**, *115*, 21249–21257.
- (73) Jeon, J.; Hsieh, C.-S.; Nagata, Y.; Bonn, M.; Cho, M. Hydrogen Bonding and Vibrational Energy Relaxation of Interfacial Water: A Full DFT Molecular Dynamics Simulation. *J. Chem. Phys.* **2017**, *147*, No. 044707.
- (74) Xu, J.; Zhang, Y.; Voth, G. A. Infrared Spectrum of the Hydrated Proton in Water. *J. Phys. Chem. Lett.* **2011**, *2*, 81–86.
- (75) Biswas, R.; Carpenter, W.; Fournier, J. A.; Voth, G. A.; Tokmakoff, A. IR Spectral Assignments for the Hydrated Excess Proton in Liquid Water. *J. Chem. Phys.* **2017**, *146*, No. 154507.

- (76) Smith, J. D.; Saykally, R. J.; Geissler, P. L. The Effects of Dissolved Halide Anions on Hydrogen Bonding in Liquid Water. *J. Am. Chem. Soc.* **2007**, *129*, 13847–13856.
- (77) Puisto, M.; Pussi, K.; Alatalo, M.; Hesp, D.; Dhanak, V. R.; Lucas, C. A.; Grunder, Y. LEED-IV and DFT Study of the Coadsorption of Chlorine and Water on Cu (100). *Surf. Sci.* **2017**, *657*, 51–57.
- (78) Futamata, M. In-situ ATR-IR Study of Water on Gold Electrode Surface. *Surf. Sci.* **1999**, *427–428*, 179–183.
- (79) Tong, Y.; Lapointe, F.; Thamer, M.; Wolf, M.; Campen, R. K. Hydrophobic Water Probed Experimentally at the Gold Electrode/Aqueous Interface. *Angew. Chem., Int. Ed.* **2017**, *56*, 4211–4214.
- (80) Perera, P. N.; Fega, K. R.; Lawrence, C.; Sundstrom, E. J.; Tomlinson-Phillips, J.; Ben-Amotz, D. Observation of Water Dangling OH Bonds Around Dissolved Nonpolar Groups. *Proc. Natl. Acad. Sci. U.S.A.* **2009**, *106*, 12230–12234.
- (81) Tomlinson-Phillips, J.; Davies, J.; Ben-Amotz, D.; Spångberg, D.; Pejov, L.; Hermansson, K. Structure and Dynamics of Water Dangling OH Bonds in Hydrophobic Shells. Comparison of Simulation and Experiment. *J. Phys. Chem. A* **2011**, *115*, 6177–6183.
- (82) Davis, J. G.; Rankin, B. M.; Gierszal, K. P.; Ben-Amotz, D. On the Cooperative Formation of Non-hydrogen-bonded Water at Molecular Hydrophobic Interfaces. *Nat. Chem.* **2013**, *5*, 796–802.
- (83) Sovago, M.; Campen, R. K.; Wurlpel, G. W. H.; Muller, M.; Bakker, H. J.; Bonn, M. Vibrational Response of Hydrogen-Bonded Interfacial Water is Dominated by Intermolecular Coupling. *Phys. Rev. Lett.* **2008**, *100*, No. 173901.
- (84) Liu, G.-K.; Zou, S.-Z.; Richter, L. J.; Moffat, T. P. Surface Structure Dependent Electrochemical Co-adsorption of Water and Sulfate on Au Investigated by SEIRAS, to be submitted for publication, 2019.
- (85) Agmon, N.; Bakker, H. J.; Campen, R. K.; Henchman, R. H.; Pohl, P.; Roke, S.; Thamer, M.; Hassanali, A. Protons and Hydroxide Ions in Aqueous Systems. *Chem. Rev.* **2016**, *116*, 7642–7672.
- (86) Chen, Y.; Okur, H. I.; Gomopoulos, N.; Macias-Romero, C.; Cremer, P. S.; Petersen, P. B.; Tocci, G.; Wilkins, D. M.; Liang, C.; Ceriotti, M.; et al. Electrolytes Induced Long Range Orientational Order. *Sci. Adv.* **2016**, *2*, No. e1501891.
- (87) Hopkins, A.; McFearin, C. L.; Richmond, G. L. SAM's Under Water: The Impact of Ions on the Behavior of Water at Soft Hydrophobic Surfaces. *J. Phys. Chem. C* **2011**, *115*, 11192–11203.
- (88) Begum, R.; Matsuura, H. Conformational Properties of Short Poly(oxyethylene) Chains in Water Studied by IR Spectroscopy. *J. Chem. Soc., Faraday Trans.* **1997**, *93*, 3839–3848.
- (89) Matsuura, H.; Fukuhara, K. Vibrational Spectroscopic Studies of Conformation of Poly(oxyethylene). II. Conformation-spectrum Correlations. *J. Polym. Sci., Part B: Polym. Phys.* **1986**, *24*, 1383–1400.
- (90) Shephard, J. J.; Bremer, P. J.; McQuillan, A. J. Structure and Conformation in Mixtures of Methyl-Terminated Poly(ethylene oxide) and Water. Principal Component Analysis and Band Fitting of Infrared Absorptions. *J. Phys. Chem. B* **2009**, *113*, 14229–14238 and references therein.
- (91) Rubinson, K. A.; Meuse, C. W. Deep Hydration: Poly(ethylene glycol)  $M_w$  2000–8000 Da Probed by Vibrational Spectroscopy and Small Angle Neutron Scattering and Assignment of  $\Delta G^\circ$  to Individual Water Layers. *Polymers* **2013**, *54*, 709–723 and references therein.
- (92) Miyazawa, T.; Fukushima, K.; Ideguchi, Y. Molecular Vibrations and Structure of High Polymers III, Infrared Spectra, Normal Vibrations, and Helical Conformation of Polyethylene Glycol. *J. Chem. Phys.* **1962**, *37*, 2764–2776.
- (93) Yoshihara, T.; Tadokoro, H.; Murahashi, S. Normal Vibrations of the Polymer Molecules of Helical Conformation. IV. Polyethylene Oxide and Polyethylene-d4 Oxide. *J. Chem. Phys.* **1964**, *41*, 2902–2911.
- (94) Xu, K.; Lu, H.; Kinder, E. W.; Seabaugh, A.; Fullerton-Shirey, S. K. Monolayer Solid-State Electrolyte for Electric Double Layer Gating of Graphene Field-Effect Transistors. *ACS Nano* **2017**, *11*, 5453–5464.
- (95) Zobnina, V. G.; Kosevich, M. V.; Chagovets, V. V.; Boryak, O. A.; Kulik, A. N.; Gomory, A. Stable Associates of Polyether Oligomers with Chlorine Anion as Revealed by the Data of Electrospray Mass Spectrometry and Molecular Dynamics. *J. Anal. Chem.* **2011**, *66*, 1341–1347.
- (96) Goldbach, S.; Messing, W.; Daenen, T.; Lapique, F. Coupled Effects of Chloride Ion and Branched Chained Polypropylene Ether LP-1 on the Electrochemical Deposition of Copper from Sulfate Solutions. *Electrochim. Acta* **1998**, *44*, 323–335.
- (97) Gallaway, J. W.; West, A. C. PEG, PPG and Their Triblock Copolymers as Suppressor in Copper Electroplating. *J. Electrochem. Soc.* **2008**, *155*, D632–D639.
- (98) Gallaway, J. W.; Willey, M. J.; West, A. C. Copper Filling of 100 nm Trenches Using PEG, PPG and a Triblock Copolymer as Plating Suppressors. *J. Electrochem. Soc.* **2009**, *156*, D287–D295.
- (99) Mendez, J.; Akolkar, R.; Landau, U. Polyether Suppressors Enabling Copper Metallization of High Aspect Ratio Interconnects. *J. Electrochem. Soc.* **2009**, *156*, D474–D479.
- (100) Xiao, N.; Li, N.; Cui, G.; Tian, D.; Yu, S.; Li, Q.; Wu, G. Triblock Copolymers as Suppressor for Microvia Filling via Copper Electroplating. *J. Electrochem. Soc.* **2013**, *160*, D188–D195.
- (101) Ryan, K.; Dunn, K.; van Eidsen, J.; Adolf, J. Properties of PEG, PPG and Their Copolymers: Influence on Copper Filling of Damascene Interconnects. *J. Electrochem. Soc.* **2013**, *160*, D3186–D3196.
- (102) Xiao, N.; Li, D.; Cui, G.; Li, N.; Li, Q.; Wu, G. Adsorption Behavior of Triblock Copolymer Suppressors During Copper Electrodeposition. *Electrochim. Acta* **2014**, *116*, 284–291.
- (103) Schmolka, I. R. A Review of Block Polymer Surfactants. *J. Am. Oil Chem. Soc.* **1977**, *54*, 110–116.
- (104) Bodratti, A. M.; Sarkar, B.; Alexandridis, P. Adsorption of Poly(ethylene oxide)-containing Amphiphilic Polymers on Solid-liquid Interfaces: Fundamentals and Applications. *Adv. Colloid Interface Sci.* **2017**, *244*, 132–163.
- (105) Gonzalez-Lopez, J.; Alvarez-Lorenzo, C.; Taboada, P.; Sosnik, A.; Sandez-Macho, I.; Concheiro, A. Self-Associative Behavior and Drug-Solubilizing Ability of Poloxamine (Tetronic) Block Copolymers. *Langmuir* **2008**, *24*, 10688–10697.
- (106) Dong, J.; Armstrong, J.; Chowdhry, B. Z.; Leharne, S. A. Thermodynamic Modeling of the Effect of pH Upon Aggregation Transitions in Aqueous Solutions of the Poloxamine T701. *Thermochim. Acta* **2004**, *417*, 201–206.
- (107) Su, Y. L.; Wang, J.; Liu, H. Z. Formation of a Hydrophobic Microenvironment in Aqueous PEO-PPO-PEO Block Copolymer Solutions Investigated by Fourier Transform Infrared Spectroscopy. *J. Phys. Chem. B* **2002**, *106*, 11823–11828.
- (108) Samuel, A. Z.; Umaphathy, S. Energy Funneling and Macromolecular Conformational Dynamics: A 2D Raman Correlation Study of PEG Melting. *Polym. J.* **2014**, *46*, 330–336.
- (109) Moffat, T. P.; Wheeler, D.; Josell, D. Electrodeposition of Copper in the SPS- PEG-Cl Additive System. *J. Electrochem. Soc.* **2004**, *151*, C262–C271.
- (110) Kunitake, M.; Batina, N.; Itaya, K. Self-Organized Porphyrin Array on Iodine-Modified Au(111) in Electrolyte Solutions: In Situ Scanning Tunneling Microscopy Study. *Langmuir* **1995**, *11*, 2337–2340.
- (111) Lutter, J. C.; Wu, T.; Zhang, Y. Hydration of Cation: A Key to Understanding of Specific Cation Effects in Aggregation Behaviors of PEO-PPO-PEO Triblock Copolymers. *J. Phys. Chem. B* **2013**, *117*, 10132–10141.